

Fizra Khan

**A 2D MODEL OF CORTICAL SPREADING DE-
PRESSION PROPAGATION USING NEURAL
FIELD FRAMEWORK: A COMPUTATIONAL
STUDY**

Faculty of Medicine and Health Technology
Master's Thesis
December 2025

ABSTRACT

Author : A 2D Model of Cortical Spreading Depression Propagation Based on Neural Field Framework: A Computational Study
Master's Thesis
Tampere University
Biomedical Sciences and Engineering
December 2025

Cortical spreading depression (CSD) is a biological event that arises as a slow wave of neuronal and glial depolarization across the cortex, in response to brain injury. The key neurochemical disturbance responsible for it is elevated potassium concentration in extracellular space. It is associated with injuries such as traumatic brain injury, subarachnoid haemorrhage and migraine. CSD induces conditions in the cortex that are physiologically unfavourable and is highly prone to recurrence causing severe damage to neurons.

Computational modelling approach has been widely used to investigate underlying mechanisms of CSD. Cell-based models are commonly used in computational neuroscience to understand biophysical details of a phenomenon. However, they become increasingly complex and computationally inefficient when extended to the spatial domains required for CSD like propagation.

Mean-field models, more specifically neural field models, provide a solid framework to model spatially extensive patterns and temporal evolutions of wave fronts without complexity. This is quite useful for capturing large-scale cortical phenomena with reduced computational burden.

The main objective of this thesis was to develop a two-dimensional (2D) model of CSD propagation based on neural field framework. The model was developed as an extension of a one-dimensional model developed by Baspinar et al. The original model includes extracellular potassium dynamics and its effect on the firing of neuronal populations within the framework.

This was achieved by implementing the neural field model on a 2D grid where each node represented a neural field unit. The equations of the model on individual node describe the coupled dynamics of two main neuronal populations, excitatory and inhibitory. Potassium concentration dependent sigmoidal transfer function was used to model the firing rate. A 2D exponential spatial kernel was used for weighted sum of signals from other populations. The stimulus was applied at three different locations to understand the spatial and temporal evolution of potassium and population dynamics in a 2D space. CSD speed was calculated with threshold-based front detection. Parameters such as number of nodes, distance between nodes and time constant were explored to find similar speed as control.

Radial curvatures and distinct ring-like patterns emerged as a result in spatial distribution. The firing rate of excitatory and inhibitory population exhibited potassium modulated behavior as modelled by Baspinar et al. The CSD speed closest to control speed (2.2 mm/min) was found to be 2.35 mm/min.

In conclusion, the 2D model was successful in capturing the CSD propagation based on potassium dynamics. The 2D model could serve as a foundation to simulate brain source activity and project the underlying neuronal activity at electroencephalography as voltages using forward projection method. This could be beneficial in finding detectable patterns in routine monitoring of CSD.

Keywords: Cortical Spreading Depression, Neural Field Framework, Neural Field Models, Mean Field Models, Neuroscience

The originality of this thesis has been verified using the Turnitin Originality Check service.

USE OF AI IN THESIS

I have utilised AI tools in my thesis:

- No
- Yes

The AI tools utilised in my thesis and their purposes are described below:

Names and versions of AI tools:

ChatGPT 5.0, ChatGPT 5.1, Perplexity AI, SciSpace

Purpose of using AI tools:

1. Information searching and brainstorming
2. Literature review
3. Minor refinement of text scripts such as vocabulary, grammar, and style for clarity

Sections where AI tools were used:

1. INTRODUCTION
2. BACKGROUND
3. MATERIALS AND METHODS
4. DISCUSSION
5. CONCLUSION

I acknowledge that I am fully responsible for the entire content of my thesis, including the parts generated by AI, and accept accountability for any violations of ethical standards in publications.

PREFACE

This thesis was completed as a fulfilment of master's degree requirement that has given me immense pleasure and challenges throughout the process. I would like to take this opportunity to extend my gratitude towards many individuals.

Firstly, I am grateful to my supervisor, Narayan Puthanmadam Subramaniam, for their continuous assistance and feedback, which were instrumental throughout the project and shaped its final form. I would also like to acknowledge and thank members of Neuro Team in Computational Biophysics and Imaging Research Group for their support. In addition, my sincere gratitude goes to Tampere University, the education system of Finland and its people, for giving me the opportunity and resources that paved the way for me to achieve a significant milestone in my life.

I am especially grateful to my mother, who has been nothing less than an inspiration and whose strength and resilience have shaped the person I am today. My sister, thank you for always being my biggest cheerleader. My heartfelt appreciation to my friends for their constant encouragement and for always seeing the best in me. In the end, I would like to commend myself for persevering through this journey despite facing countless moments of doubts.

Tampere, 30 November 2025

Fizra Khan

CONTENTS

1.INTRODUCTION	1
2.BACKGROUND	4
2.1 Pathophysiology of Cortical Spreading Depression	4
2.1.1 Role of Neurons	5
2.1.2 Role of Astrocytes	7
2.1.3 Cell Morphology and Vascular Response	9
2.2 Clinical Monitoring of Cortical Spreading Depression.....	9
2.3 Computational Approaches for Modelling Neuronal Dynamics.....	11
2.3.1 Cell Based Models	11
2.3.2 Mean field Models	12
2.4 Neural Field Framework	14
2.4.1 Types of Spatial Kernel	16
2.4.2 Parameterization and Bifurcation Analysis	19
2.5 Computational Modelling of Cortical Spreading Depression Based on Neural Field Framework	20
3.AIMS AND OBJECTIVES	21
4.METHODS.....	22
4.1 Domain	22
4.2 Neural Field Model.....	23
4.3 Model Components.....	24
4.3.1 State Variables	24
4.3.2 Spatial Kernel	25
4.3.3 Firing Rate	25
4.3.4 Effect of Potassium Concentration on Neural Population	27
4.3.5 Effect of Neural Population on Potassium Concentration	28
4.3.6 Laplacian Operator	28
4.3.7 Stimulus.....	28
4.4 Calculation of CSD speed.....	30
5.RESULTS	31
5.1 Spatial Distribution.....	31
5.2 Neuronal Firing	33
5.3 Temporal Dynamics.....	36
5.4 CSD Speed	40
6.DISCUSSION.....	42
6.1 Spatial Patterns:	42
6.2 Neural Firing and Temporal Patterns	43
6.3 CSD Speed	44
6.4 Future work	44
6.5 Limitations	46

7. CONCLUSION	47
8. REFERENCES	48
9. SUPPLEMENTARY WORK	54
9.1 EEG Forward Projection	54
9.1.1 Distribution of neuronal currents	54
9.1.2 Conduction of neuronal currents	55
9.1.3 Relationship between neuronal activity and scalp potential	55
9.2 METHOD	56
9.3 RESULTS	56

LIST OF SYMBOLS AND ABBREVIATIONS

CSD	Cortical Spreading Depression
TBI	Traumatic Brain Injury
aSAH	Aneurysmal Subarachnoid Haemorrhage
DCI	Delayed Cerebral Ischemia
ECoG	Electrocorticography
EEG	Electroencephalography
MEG	Magnetoencephalography
1D	One dimension
2D	Two dimensions
3D	Three dimensions
MRI	Magnetic Resonance Imaging
fMRI	functional Magnetic Resonance Imaging
GABA	Gamma-aminobutyric acid
Kir4.1	Inward rectifying potassium channel
GLT	Glutamate transporter
EAAT	Excitatory amino acid transporter
NO	Nitric Oxide
BOLD	Blood Oxygen Level Dependent
LSI	Laser Speckle Imaging
PRI	Pressure Reactive Index
KCL	Potassium Chloride

1. INTRODUCTION

This chapter introduces the main topic of this work. It outlines the importance of studying cortical spreading depression (CSD) in terms of its clinical relevance. It also provides a broad overview of phenomenological models and their applications. Furthermore, it introduces the broad aim of this work.

CSD is a pathophysiological phenomenon, described by Aristides Leão in 1940s that occurs in the cortical region of the brain due to ionic and neurotransmitter imbalance in the cell and extracellular space [1]. These ionic shifts cause slow propagating depolarization waves in neuronal and glial cells followed by a period of suppressed neuronal activity. CSD occurs as a secondary condition in many neurological diseases such as traumatic brain injury (TBI), aneurysmal subarachnoid hemorrhage (aSAH), stroke and migraine [2]. TBI, caused by any external mechanical pressure, leads to acute subdural hematoma or swollen hemisphere, requiring brain surgery as treatment. It has been shown that CSD occurs in about 50 - 60% of these cases as a secondary condition causing further neuronal damage [2,3]. The presence of CSD in TBI is associated with severe metabolic crisis and excessive depletion of glucose levels in the brain due to high energy demand [2]. Furthermore, the increased intracranial pressure has been linked to higher incidence of CSD in these cases resulting in high potassium and sudden depolarizations [2].

Similarly, aSAH is another lethal disease caused by the rupture of an aneurysm. Once aSAH occurs, about 25 - 30% of the patients are known to develop delayed cerebral ischemia (DCI) meaning inadequate blood perfusion in the brain [2,4]. The cause of DCI is attributed to several factors such as micro thrombosis, narrowing of arteries and CSD. The development of hypoxic (i.e., low oxygen) conditions in the brain following aSAH is considered a direct result of CSD. [4–7]

Another condition where CSD is observed is migraine. Impaired cortical activity and vascular reactivity patterns like CSD in response to hemodynamic changes have been shown in imaging modalities in patients with migraine [2]. The onset of CSD in response to neurovascular uncoupling leads to a mechanism that releases nociceptive messengers i.e. pain signals in migraine patients causing headaches [8]. Familial hemiplegic migraine (FHM) is a type of migraine with aura that causes hemiparesis i.e. paralysis of one side of the body due to genetic mutations of $Na_v1.1$ voltage-gated sodium channel

activated by SCN1A gene [9]. Other conditions where CSD has been documented are stroke and intracerebral hemorrhage [2,10,11]. CSD and seizures have also been documented to coincide with each other [12].

These observations suggest that CSD plays a main role in multiple neuronal conditions. While most of the CSD onsets are caused by prior brain injury, triggers for sudden CSD episodes are still under investigation. Furthermore, the outcome of the diseases is likely to be worsened by CSD which exacerbates metabolic stress, impairs cerebral perfusion, and promotes neuronal death [2]. This highlights the need to further understand the underlying pathophysiology of CSD to help identify the detectable patterns for early intervention.

Phenomenological models have recently gained a widespread adoption for modelling neural dynamics. These are derived from dynamical system approaches where assumptions are made at the mesoscopic or macroscopic level. They offer a simplified representation of brain dynamics by describing the aggregated behavior of neural populations and networks. These models have been used to integrate empirical data to predict, test and evaluate the behavior of neuronal networks. [13]

One such approach has been used to understand the effect of neuromodulators such as dopamine impairment on brain activity, which has been associated with Parkinson's disease and schizophrenia [14–16]. Other instances where this approach has been used are modelling of seizures, sleep and anesthesia [13,17–19]. It is evident that these approaches have received attraction in modelling diseases and pathologies that require network level description.

CSD, a disruption to biological processes, can also be examined through phenomenological models that encapsulate its large-scale propagation dynamics. One of the simplest ways to understand CSD propagation is to model the dynamics on a one-dimensional (1D) surface representing a piece of cortical tissue, using phenomenological approaches. A computational model developed by Baspinar et al. follows a similar approach [20,21].

However, the cortex exists in a volume space of skull and brain. A 1D model makes the visualization of wave propagation curvatures across the cortex difficult. Moreover, it does not account for regional differences in CSD propagation which are possible to integrate in high-dimensional surfaces. Monitoring modalities such as electroencephalography (EEG) or magnetoencephalography (MEG) record signals distributed in a volume space that require source activity to be in high dimensions. Therefore, a high-dimensional computational model of CSD is required.

In this thesis, the aim is to develop a 2D model as an extension of Baspinar et al's model built on neural field framework. This will allow us to understand spatial patterns and temporal dynamics of CSD based on region of its initiation. Moreover, this can serve as a foundation for future studies conducted to model the brain signals on scalp.

The upcoming part of the thesis discusses the relevant background regarding CSD and theoretical components needed to understand our model. The chapter also provides the rationale for their selection. In the next section, objectives pertaining to this work are outlined. This is followed by Materials and Methods section describing the population level model based on neural field framework used to model CSD. Subsequent sections provide the Results and Discussion sections to put the outputs obtained from the model, outlining the direction for future work.

2. BACKGROUND

This chapter discusses the underlying biological mechanisms in CSD phenomena on microscopic level and its monitoring. The chapter further delves into computational modelling approaches used to model neural dynamics. It explains the theoretical understanding of phenomenological models, more specifically, neural mass and neural field models. Subsequently, the modelling framework of Baspinar et al. is discussed.

2.1 Pathophysiology of Cortical Spreading Depression

CSD, a depolarization wave of the cortical neurons illustrated in Figure 1, affects the normal physiological function not only of neurons but also glial cells, alters cell morphology and microvasculature regulation in the brain [27-41]. These changes cause disturbances in maintaining the homeostasis of the brain tissue.

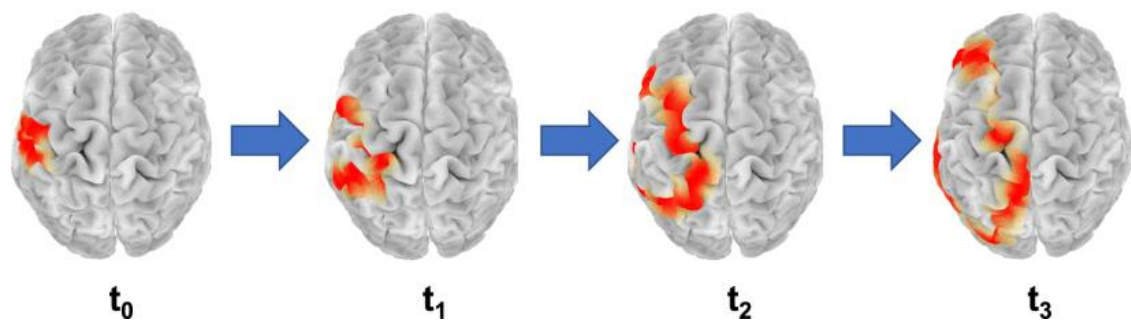


Figure 1. Example of CSD propagation over the cortex. The red circle represents the depolarization of neurons at times $t_0 < t_1 < t_2 < t_3$. Image from Chamanzar et al. [23]

The cerebral cortex comprises of billions of neurons of many types. The main subtypes discussed in this thesis are pyramidal neurons and interneurons. Pyramidal neurons are excitatory, form long-range connections with other neurons, and release glutamic acid commonly referred to as glutamate, hence, classified as excitatory glutamatergic neurons [24,25]. In contrast, interneurons form more localized connections, and release inhibitory neurotransmitter called gamma-aminobutyric acid (GABA) which classifies them as inhibitory GABAergic neurons [24,25]. The typical structure of neurons includes dendrites, cell membrane, cell body and axon as shown in Figure 2.

In normal physiological function, neurons maintain homeostasis by regulated interplay between sodium (Na^+) and potassium (K^+) ions across cell membrane. Neurons fire action potentials generated by the coordinated opening and closing of voltage-gated Na^+ and K^+ channels. The influx of Na^+ ions depolarize the membrane, followed by K^+ efflux in the extracellular space that repolarizes and restores the resting membrane potential.

This electrical event leads to current generation in the cell body and its conduction through the axon. [26]

In addition to voltage-gated Na^+ and K^+ channels, the depolarization event opens voltage-gated calcium (Ca^{2+}) channels which cause (Ca^{2+}) to release synaptic vesicles to release a neurotransmitter. The neurotransmitter carries the signal to excite or inhibit from one neuron (presynaptic) to another neuron (postsynaptic) via synaptic cleft [27]. Postsynaptic neurons receive and integrate thousands of excitatory postsynaptic potentials and inhibitory postsynaptic potentials, with dendritic structure shaping how these inputs are weighted and summed [28].

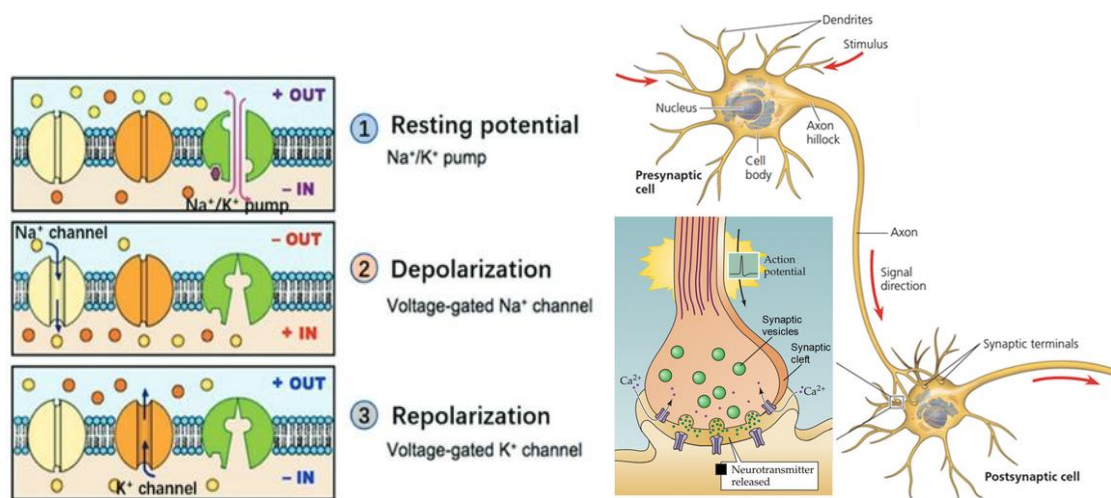


Figure 2. Left side shows the ion channel dynamics for generation of action potential. The membrane maintains resting potential with ionic balance across cell membrane with the help of Na^+/K^+ pump. Once the Na^+ channel is opened, the movement of Na^+ into the cell changes membrane potential corresponding to depolarization phase. Later, the opening of K^+ channels leads the movement of K^+ ions out of the cell membrane corresponding to repolarization phase. Right side shows signal transmission between presynaptic and postsynaptic neurons. When the action potential, generated at the axon hillocks, reaches axon terminal, it triggers the release of Ca^{2+} ions affecting the release of neurotransmitter in the synaptic cleft. Image adapted from Tang J et al. [29]

2.1.1 Role of Neurons

In the event of CSD, the function of neurons is impacted. When a brain region undergoes damage due to injury, the main physiological mechanism involved in CSD is initiated due to massive energy failure and anoxic conditions. The mechanism is triggered in glutamatergic neurons first and due to their unusual excitatory firing behavior, GABAergic neurons are affected in a similar manner.

At the injured site, impaired adenosine triphosphate (ATP) production, a molecule required for the pump activity of ions, hinders the normal physiological function of Na^+/K^+

ATPase ion pump [30]. The impacted neuron abnormally depolarizes by changing its membrane potential from -70 mV to -10 mV as potassium ions leave the cells and start to accumulate in the extracellular space [12,22,31]. This overwhelms the ability of ion pumps and channels to return to its resting membrane potential. Moreover, depolarization leads to activation of voltage-gated channels for Ca^{2+} ions mainly P/Q type channels which facilitate the release of glutamate from synaptic vesicles [32]. Glutamate activates N-methyl-D-aspartate (NMDA) receptors of the post synaptic neuron allowing further influx of cations into the cell. This depolarizes the post synaptic neuron further releasing glutamate and accumulating potassium ions, increasing glutamatergic activity [33]. This mechanism is perpetuated in the adjacent neurons, and a wave of depolarization arises across the cortex propagating CSD followed by inhibited neuronal activity.

The hyperexcitability of GABAergic neurons, due to pyramidal neuronal firing, only leads to more potassium accumulation. Even though the interneurons are maximally activated, the release of inhibitory GABA has a mild effect on pyramidal activity and overall neuronal hyperexcitability. [34]

If this mechanism persists and causes recurrence of CSD, the risk of neuronal damage and apoptosis becomes high as the metabolic requirements increase. Usually, CSD propagates at the speed of 2 - 5 milli meter per minute (mm/min) [1], but tissue injury and genetic factors can affect its speed. In this work, only the increase in potassium concentration is modelled.

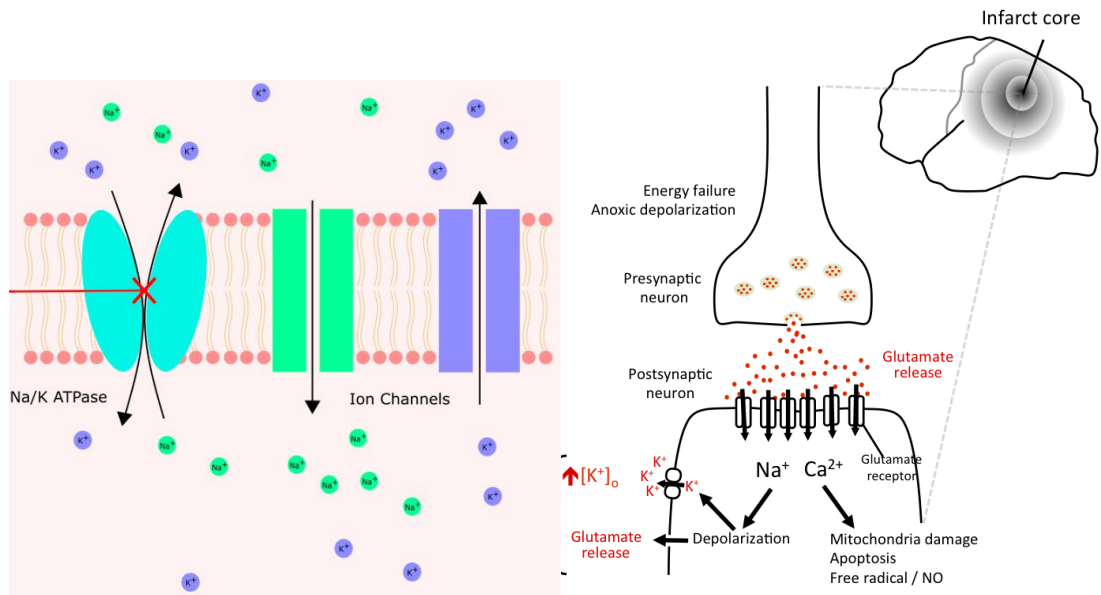


Figure 3. CSD initiation and propagation mechanisms in response to neuronal injury. Once the neuron is impacted, its ability to maintain homeostasis is impacted. On the left side, the impaired activity of Na^+/K^+ ion pump (in blue) is shown. This affects the uptake of K^+ ions (purple) back into the cell after influx of Na^+ ions (green) into the cell. On the right side, the impact on the adjacent neurons is shown. The depolarization of presynaptic neuron triggers neurotransmitter (glutamate shown in red) release mechanism. Glutamate attaches to glutamate receptors on post synaptic neurons inducing action potential. This further contributes to potassium accumulation and glutamate excitotoxicity, both shown in red, leading to wave of depolarization across the cortex. Images from Hill et al. [30] and Aizawa H. [35]

2.1.2 Role of Astrocytes

Glial cells, mainly astrocytes, support neurons in various ways and become excitable by producing intracellular calcium transients and waves. Astrocyte forms a tripartite synapse with pre and post synaptic neurons and support the regulation of neurons. They form an astrocytic network by connecting at the gap junction and communicate with each other through it. Some of the most important roles of astrocytes are, uptaking of extracellular potassium and glutamate, and converting glucose coming from the bloodstream into energy source for neurons. [36]

The potassium uptake is regulated by inward rectifying potassium channel (Kir4.1), which is highly expressed in astrocytes, in normal conditions, to maintain homeostasis. The potassium ions follow the electrochemical gradient via Kir4.1 channel. When CSD occurs and potassium concentration increases due to hyperexcitability of neurons, astrocyte begins the uptake but soon loses its effectiveness due to decreased conductance of Kir4.1 channel. In result, the activity of sodium potassium pumps (Na^+ / K^+ ATPase activity) increases to restore the gradient. However, due to high potassium concentration, this activity is also impaired leading to inability in clearance. [37–40]

Astrocytes take up glutamate from the extracellular space through glutamate transporters (GLT), predominantly excitatory amino acid transporters (EAATs), EAAT1 (GLAST) and EAAT2 (GLT-1). This uptake is performed by converting glutamate into glutamine through biological reaction known as glutamine synthetase. CSD impairs this activity due to excessive glutamate released by the neurons causing high demand and overwhelming astrocytes uptake ability. Therefore, instead of uptaking, these transporters produce reversal effects contributing to excitotoxicity. [37,39,40]

Moreover, tumor necrosis factor α (TNF- α) is a pro-inflammatory cytokine which is released during CSD. In astrocytes, TNF- α is known to downregulate GLT-1, affecting glutamate clearance. [37,41]

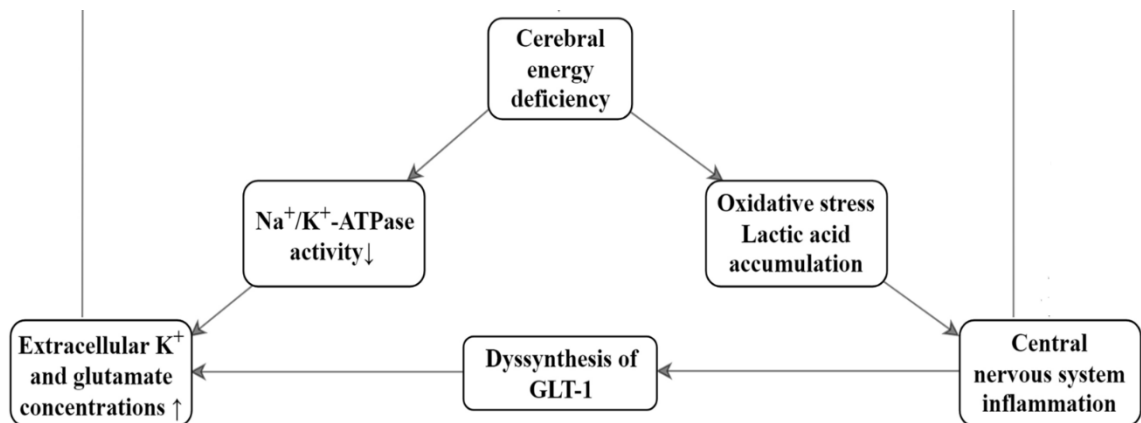


Figure 4. Astrocytes perform the buffering of the K^+ ions and glutamate via Kir4.1 channel and GLT1. Due to CSD induced energy deficiency, this activity is compromised. Furthermore, it increases the production of lactic acid by astrocytes. This leads to release of inflammatory cytokines leading to downregulation of GLT1. This contributes to the increase in extracellular and K^+ concentrations. Image adapted from Yang et al. [37]

Moreover, this massive shift in ionic imbalance drives increase in energy demand not fulfilled by blood glucose alone. Astrocyte facilitates this by catabolizing glycogen for rapid glycolysis. Consequently, the accumulation of excessive lactic acid causes hypoxia which gives rise to severe metabolic dysfunction in the nervous system. In normal conditions, in addition to glutamate, nitric oxide (NO) and arachidonic acid are released that allow vasodilation and increase local blood flow. The disproportionate increase of lactate makes the environment acidic, which is not thriving to produce NO leading to poor perfusion. Regions affected by poor perfusion are more vulnerable to repeated CSDs which may create ischemic conditions. [37,42]

2.1.3 Cell Morphology and Vascular Response

In addition to the influx of ions in the face of CSD, the increased osmolarity drive in intracellular spaces alters the morphology of neural and glial cells. In neurons, the movement of water molecules occurs primarily through osmotic gradients, whereas in astrocytes the movement of water is facilitated by aquaporin-4 channels that transport water. These effects compromise the cellular structure and produce swelling of the cells. This ultimately results in extracellular space shrinkage, and recurrent CSD drives degeneration of dendritic spines. [37,43,44]

The onset of CSD profoundly impacts the vasculature of the brain eliciting triphasic hemodynamic response, i.e. initial vasoconstriction, a brief vasodilation, and prolonged vasoconstriction. With recurrent CSDs, the oligemia i.e. reduction in cerebral blood flow and vasoconstrictions become pronounced and persistent leading to energy depletion. The feedback loop exacerbates the brain damage of neurons and cerebral microvasculature. CSD also induces cytotoxic edema i.e. cell swelling which disrupts the blood brain barrier and causes subsequent vasogenic edema. These processes cause further hypoperfusion, promote inflammation and perpetuate tissue damage. Moreover, CSD contributes to penumbral expansion following stroke or traumatic injury leading to propagating neural and glial depolarization beyond the primary affected region. [45,46]

2.2 Monitoring of Cortical Spreading Depression

Due to numerous detrimental effects of CSD, it is imperative to identify and monitor CSD in neurointensive care and neurosurgical settings. CSD is defined as a slow depolarizing wave which poses challenges in its detection. Subdural electrocorticography (ECoG) is the most widely used invasive method for monitoring CSD [47]. In ECoG, CSD is detected as propagating slow potential change reflected in negative direct current (DC) shift [48]. This is succeeded by suppressed activity of high frequency (0.5 - 70 Hz) lasting for 5-30 mins in injured cortex [11,48]. This noninvasive method makes monitoring CSD difficult without craniotomy which is not feasible in all cases and poses many surgical risks. Other invasive methods include laser speckle imaging (LSI) and pressure reactive index (PRI) [47].

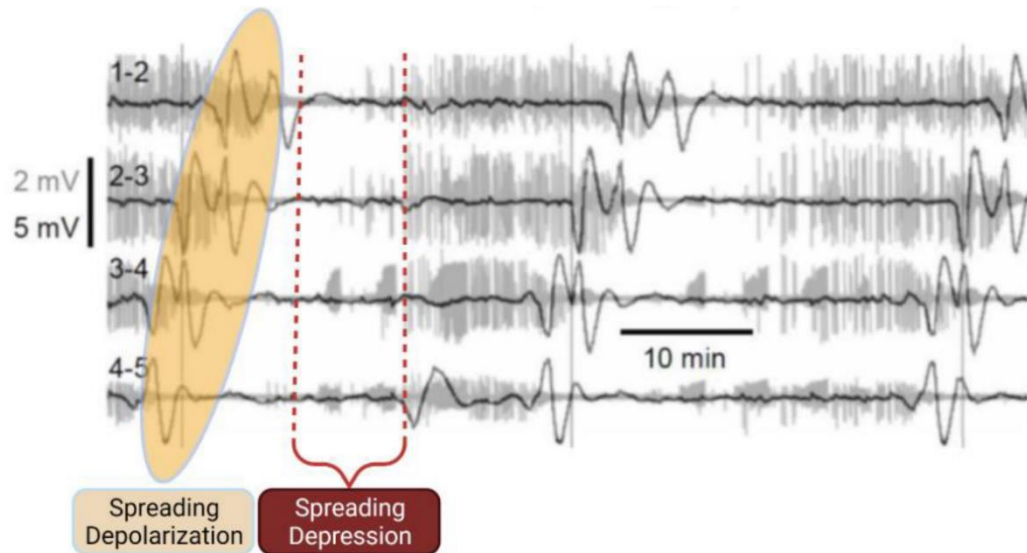


Figure 5. Detection of CSD in Electrocoorticography (ECoG). The negative deflection corresponding to depolarization is shown at 4 different electrodes. Depolarization occurs at different times at each electrode indicating its movement from one region to another in time. The depolarization wave is emphasized by orange block and is followed by the suppression of neural activity emphasized with red block. Image adapted from Mehra et al. [5]

Additionally, detection of CSD has been attempted via non-invasive methods such as EEG and MEG [47]. On EEG, CSD appears as wavefronts i.e. broken segments of propagating wave which can evolve or combined with other wavefronts [23]. Moreover, MRI (Magnetic Resonance Imaging) / fMRI (functional MRI) allows the monitoring of hemodynamics in CSD and is based on blood oxygen level dependent (BOLD) signals [47].

However, detection of CSD via these methods is not straightforward. Non-invasive techniques, such as EEG, lack the spatial and temporal resolutions required to detect slow DC shifts and propagating depolarization waves observed during CSD. The volume conduction in EEG due to different head tissue conductivities and geometry blurs the spatial characteristics of CSD waves. Moreover, injured skull and electrodes artifacts make it challenging for detection of wave propagation in EEG for continuous monitoring in clinical setting. [23,47,49]

In experimental in vivo or in vitro studies involving CSD, the initiation and propagation is studied using potassium chloride (KCL) to externally drive the potassium concentration in extracellular space [50]. ECoG is mainly used for recording in-vivo data and CSD propagation. However, other methods such as MRI, optogenetics and optical imaging via fluorescent microscopy are also employed [3,20,42]. This enables the investigation of threshold of initiation and observe the effect of different KCL concentrations on wave propagation.

2.3 Computational Approaches for Modelling Neuronal Dynamics

Computational neuroscience has progressed over the years and yielded different approaches to understand underlying functions of brain cells [51]. Neuron dynamics can be observed in two ways to model them mechanistically, bottom-up and top-down.

The bottom-up approach allows building the model from complex interactions at biophysical level such as ion channel dynamics, synaptic transmission and cellular interactions. The models that capture single cell dynamics with detailed mathematical models of neurons or small networks, are referred to as cell-based models. In contrast, top-down approach looks at the macroscopic details and infers the microscopic structural and functional dynamics of brain regions. The models that capture this are generally referred to as mean field models. [52]

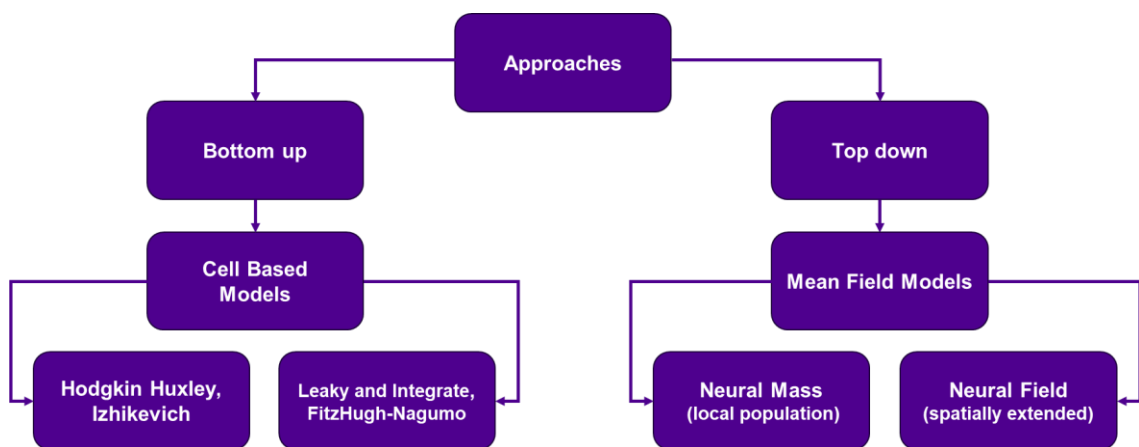


Figure 6. Hierarchy of modelling approaches and respective models for neural dynamics. Bottom-up approach involves models that are biophysically detailed such as Hodgkin-Huxley and others. Top-down approach involves models that show aggregated dynamics at the population level such as mean-field models

2.3.1 Cell Based Models

Cell based models offer a high dimensional representation of neurons with biological realism. This allows their adaptation to model wide range of brain disorders and neurological functions. Hodgkin-Huxley model, Izhikevich model, integrate-and-fire model, adaptive exponential integrate-and-fire, Fitzhugh-Nagumo model are some examples that incorporate mathematical description of membrane potentials, ion currents and channel dynamics that give rise to action potential. To capture structural characteristics, multicompartment models also exist. NEURON, NEST, The Virtual Brain, and BRIAN

are some standardized simulator packages that can be utilized to employ these models. [53–59]

Indeed, CSD and its propagation have been studied using biophysical models. For instance, Desroches et al. have developed a pyramidal and interneuron coupled model to study the role of inter-neurons in the initiation of CSD. This model showed that the intense firing of interneurons led the further increase of potassium accumulation causing the onset of CSD that aligns with the mechanisms established by experimental studies. [60]

Another model created by Conte et al. attempted to understand the biological processes in neuron and astrocyte with a mathematical model. The main goal of this was to explore the role of sodium glutamate transporters and sodium potassium ATP pumps in recurrent spreading depression and its propagation. [61]

It is important to note that in the above mentioned studies, among others [62,63] primarily used Hodgkin-Huxley based models which are biophysically detailed and provide flexibility. The propagation of CSD is a global event which involves the whole brain with thousands of neurons organized across the cortex. Therefore, if these models are extended to population or cortex level modelling, they become extremely complex and computationally challenging. Moreover, the magnitude of neural activity differs heavily when moving towards multiscale modelling which is difficult to capture with biophysical models. The limitations and challenges posed by biophysical models can be overcome by mean field models.

2.3.2 Mean field Models

Mean field models are widely used in physics due to their ability to reduce the interactions between large number of particles into statistical properties leading to much simpler and comprehensible explanations [64,65]. Similarly, this approach can be applied to a large network of neurons in the brain to describe their overall function.

The mean field approach to neurons was first provided by Wilson and Cowan in 1970s, describing the average behavior of populations based on their synaptic characteristics such as excitatory or inhibitory [66]. These models help in bridging the gap between microscopic and macroscopic brain function. The two main types based on neural field approach are neural mass models and neural field models.

Neural mass model (NMM) was originally defined to explain the mean activity of local neurons over time. The model comprises of two state variables for neuronal populations, pyramidal neurons (E) and interneurons (I), describing the mean membrane potential of

a population. Each state variable receives an input as presynaptic potential from other populations, and it converts it into the average firing rate (f) of the population using a transfer function such as sigmoid [66]. The model equations are given in equations 1 and 2.

$$\tau_E \frac{da_E}{dt} = -a_E + (1 - ra_E) f_E [W_{EE} a_E - W_{EI} a_I + i_E(t)] \quad (1)$$

$$\tau_I \frac{da_I}{dt} = -a_I + (1 - ra_I) f_I [W_{IE} a_E - W_{II} a_I + i_I(t)] \quad (2)$$

In the above equations, adapted from [61], $-E$ and $-I$ are decay terms, r is the constant, w_{EE} (excitatory \rightarrow excitatory), w_{EI} (excitatory \rightarrow inhibitory), w_{IE} (inhibitory \rightarrow excitatory), w_{II} (inhibitory \rightarrow inhibitory) connection weights between two populations, i_E and i_I are external inputs to respective populations. This coupling is represented in Fig 7.

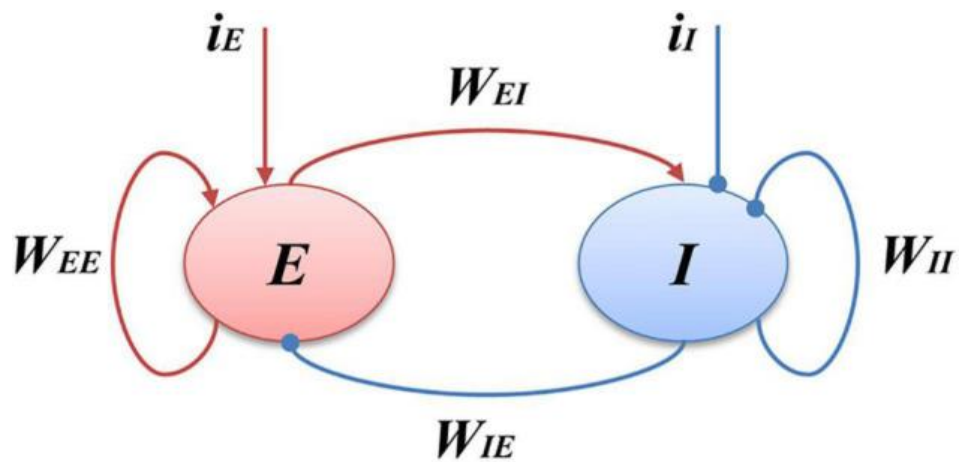


Figure 7. Coupling dynamics of Neural Mass Model equations. The equations represent two neuronal population types, excitatory (E) in red and inhibitory (I) in blue. The neurons form connections with both types of neurons in the cortex, represented as weights (W) with red and blue arrows. External inputs to the populations E and I are given as i_E and i_I respectively. Image from Li et al. [67]

Since their definition, NMMs have been extended and are extensively used in simulating EEG, MEG and fMRI signals. They are widely used in computational neuroscience field and are suitable for studying diseases, like epilepsy, which are easily observable on EEG. [68–70]

NMMs are quite useful to study local temporal dynamics of populations but do not incorporate spatial characteristics which are required for travelling waves on the cortex and CSD like propagations. Therefore, they have been expanded by many, for different purposes, but Amari was the first to give generalized spatial formulation of the neural activity continuum initially given by Wilson and Cowen [71].

2.4 Neural Field Framework

Neurons are independent multicompartement entities embedded in three-dimensional space of the brain. In neural field framework given by Amari, the approximation regarding its spatiotemporal dynamics is reduced to 2D such as a cortical sheet where neurons are treated as bulk entity by taking their average based on shared characteristics. [71,72]

The state variables define the mean membrane potential of a population (excitatory or inhibitory in general) dictated by the signal i.e. mean firing rate of other populations like in neural mass model. However, the difference is in the way it receives a signal, since it depends on the type of population, at which distance it's situated, and the amount of time passed since the signal arrived. Now, the equation combining all these components is given in equation 3:

$$v_a(x, t) = \int_{-\infty}^t \psi(t - T) I_a(x, T) dT \quad (3)$$

In equation 3, taken from [71], $v_a(x, t)$ is the mean membrane potential of population a , $\psi(t - T)$ is a temporal kernel adjusting the magnitude of the incoming signal which decays instantly, and $I_a(x, T)$ is the signal arriving from other neuronal populations at population a . It is a convolution term given as:

$$I_a(x, T) = \sum_b \int_{\Omega} w_{a,b}(x - X) f_b(u_b(X, T)) dX + q_a(x, T), \quad (4)$$

where, Ω indicates the spatial domain such as 2D sheet of the cortex, $w_{a,b}(x - X)$ is a homogenous spatial kernel which defines the mean synaptic connectivity from population b at point X to population a at point x based on distance. f_b is the incoming signal as a mean firing rate from population b generally given as a logistic sigmoid transfer function describing the response of neurons to increasing mean membrane potential. $q_a(x, T)$ is any external input other than cortex. [71]

The transfer function for f_b is given in equation 4:

$$f_b(u_b) = \frac{F_b}{1 + \exp[-\lambda_b(u_b - \theta_b)]}, \quad (5)$$

where F_b is the maximum firing rate of population b , u_b is the mean membrane potential of population, while λ_b and θ_b are the slope of u_b and threshold for F_b [71].

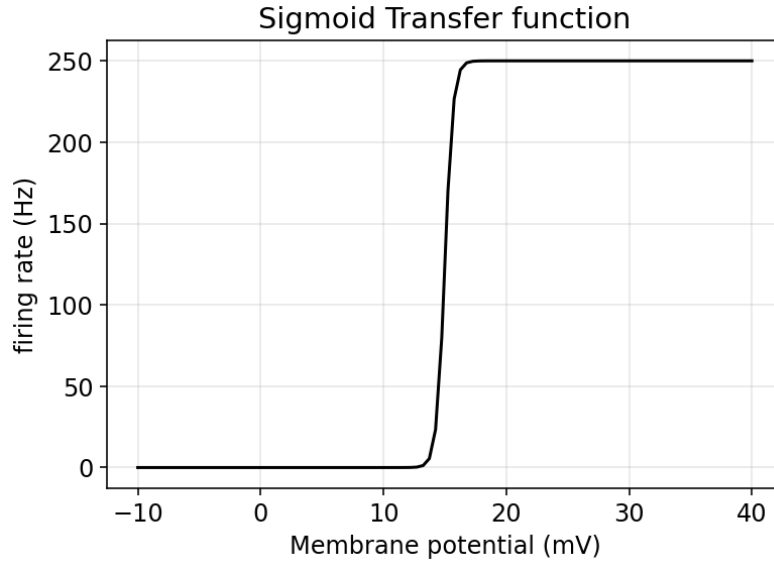


Figure 8. A logistic sigmoid function with threshold (θ_b) = 15mV, maximum firing rate (F_b) = 250 Hz and slope (λ_b) = 3mV.

The temporal kernel in equation 3 can be modelled with Heaviside step function $\theta(t)$ to incorporate the instantaneous and decaying incoming signal, and membrane time constant τ_a representing how quickly neural population returns to its resting state [71]. This can be given as:

$$\psi_a(t) = \theta(t) \frac{1}{\tau_a} e^{-\frac{t}{\tau_a}} \quad (6)$$

After putting equations 4 and 6 in equation 3, we get:

$$\tau_a \frac{\partial u_a(x, t)}{\partial t} = -u_a(x, t) + \sum_b \int_{\Omega} w_{a,b}(x - X) f_b(u_b(X, t)) dX + q_a(x, t) \quad (7)$$

Equation 7 is the basic form of neural field model for one neural population. It has been modified by researchers to investigate different neuron interactions and behavior at the macroscopic level.

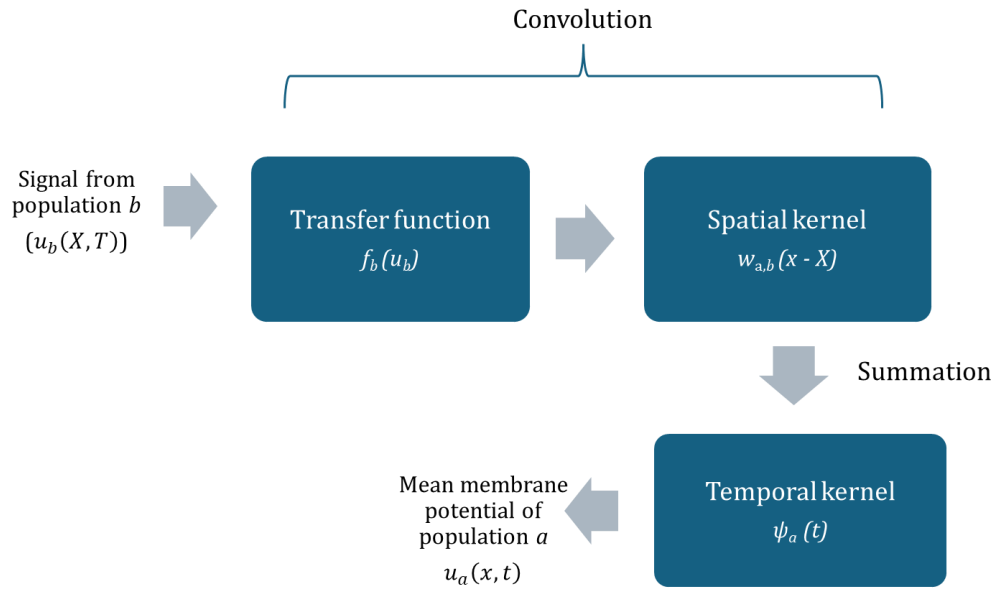


Figure 9. Block diagram of Neural Field Framework. A signal comes from presynaptic population b situated at point X and time T to population a . This signal goes through a transfer function such as sigmoid and convolves with a spatial kernel to determine the weight of the signal based on its distance from population a . The sum of incoming signals from all other populations including population b at all points undergoes temporal kernel to adjust for delay in response of population a . The final output is the mean membrane potential of population a situated at point x and time t .

2.4.1 Types of Spatial Kernel

The spatial kernels in neural field model define the synaptic connectivity between neural populations. The connectivity is expressed as the difference between distance between two populations. [71]

Some kernels explicitly model the balance between excitation and inhibition while others are represented only in terms of excitatory interactions.

Exponential Kernel:

It captures the exponential decay of synaptic strength between neuronal populations. It incorporates decaying excitation based on the width (σ) without integrating any inhibition. The equation is given in equation 8:

$$w_{(a,b)}(x) = \frac{1}{2} e^{-\frac{|x|}{2\sigma^2}} \quad (8)$$

Gaussian Kernel:

The kernel only accounts for influence of one population over others therefore, no inhibition information is encoded in it. The kernel is derived from normal distribution with zero mean. It is given in equation 9 as the probability density function where variance or width of strong connectivity (σ). [73]

$$w_{(a,b)}(x) = g_{0,\sigma} = \frac{1}{\sigma\sqrt{2\pi}} e^{-\frac{x^2}{2\sigma^2}} \quad (9)$$

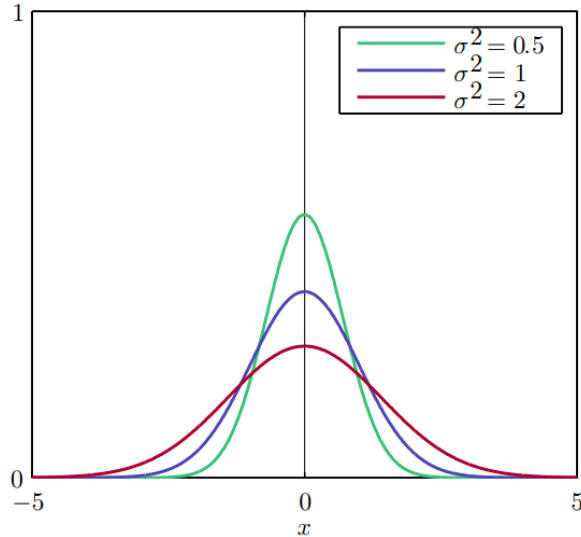


Figure 10. 1D Gaussian Kernel demonstrated with three different widths (σ). Y-axis demonstrates the kernel amplitude i.e. connectivity strengths with other populations, and x-axis represents the spatial domain of neural fields. The connectivity between neural populations under the width is nonzero while outside the width is zero. The connectivity with higher width ($\sigma^2 = 2$) shown in red has wide bell curve indicating wide range of neighboring populations are contributing to the incoming signal. While at the narrow bell curve ($\sigma^2 = 0.5$) shown in green, low range of neighboring populations are contributing to the incoming signals. Image from Loomp O. [73]

Mexican Hat Kernel:

Given by Amari, Mexican hat incorporates the balance between excitation and inhibition balance, a neuronal interaction found in cortical tissues. It is essentially the difference between the two gaussian kernels with different widths for excitation (σ_1) and inhibition (σ_2). In the kernel, the values are positive near zero and negative at the distance. [72,74]

Equation 10 gives its formulation.

$$w_{(a,b)}(x) = g_{0,\sigma_1} - g_{0,\sigma_2} \quad (10)$$

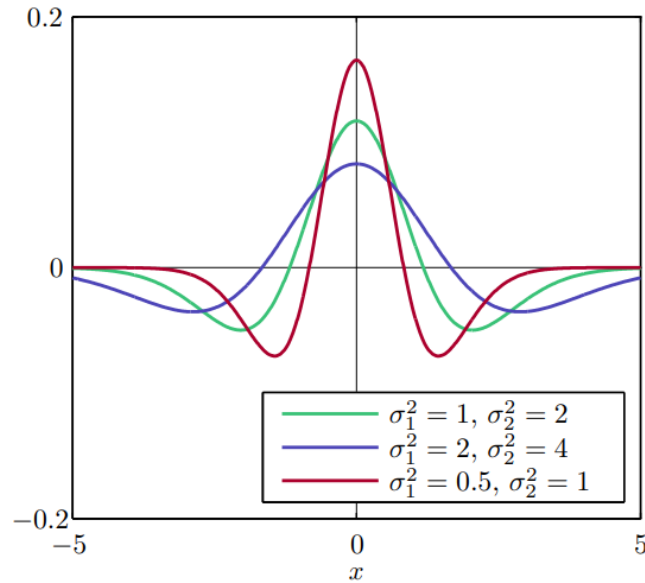


Figure 11. 1D Mexican Hat Kernel demonstrated with three different widths for excitation and inhibition. Y-axis represents the kernel amplitude i.e. connectivity strengths with other populations and x-axis represents the spatial domain of neural fields. The kernel has a central positive peak corresponding to excitatory signal and surrounding lobes corresponding to inhibitory signal. The kernel with the highest widths ($\sigma_1^2 = 2, \sigma_2^2 = 4$) shown in blue has wide spread of neighboring populations contributing to the excitatory and inhibitory signal. While the lowest width $\sigma_1^2 = 0.5, \sigma_2^2 = 1$ shown in red has narrow spread of neighboring populations contributing to the excitatory and inhibitory signal. Image from Loomp O. [73]

Wizard Hat

In the wizard hat kernel, the excitation is localized based on σ and the connectivity value is sharp at the origin while the values are negative, encoding inhibition, or zero at all the other places of interaction. [73,74]

It is given in equation 11:

$$w_{(a,b)}(x) = (1 - |\sigma x|)e^{-|\sigma x|} \quad (11)$$

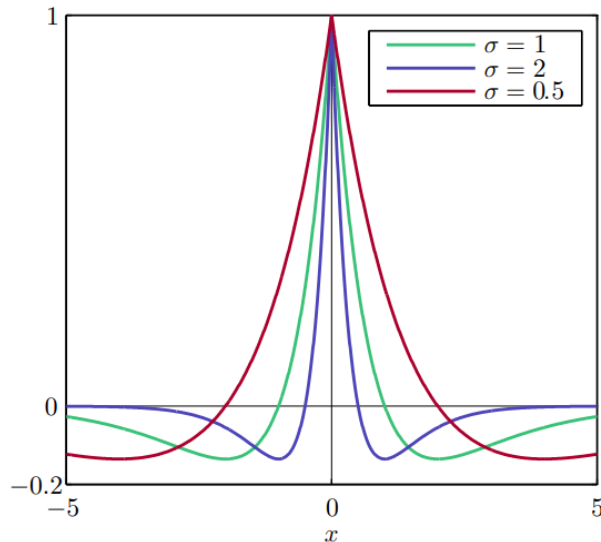


Figure 12. 1D Wizard Hat kernel demonstrated with three different widths. Y-axis represents the kernel amplitude i.e. connectivity strengths with other populations, and x-axis represents the spatial domain of neural fields. The kernel has a sharp point at the origin, indicating high local connectivity and decreasing connectivity with increasing distance, represented as negative surrounding lobes. High width ($\sigma = 2$) shown in blue, has narrow range of populations contributing to excitation and inhibition. Low width ($\sigma = 0.5$) shown in red has wide spread of neighboring population contributing to excitation and inhibition. The peak is sharp at 1 for all σ parameters and it has the opposite effect from Mexican Hat kernel on the spread. Image from Loomp O. [73]

2.4.2 Parameterization and Bifurcation Analysis

Bifurcation is a characteristic of any dynamical system including neural field models, and its systemic analysis gives insights into the model's behavior. It serves as a useful method to understand transitions in non-linear systems. Using this, the shift in the model from one state to another by identifying its bifurcation points can be studied. [75]

The behavior of a neural field model can be examined by changing the key parameters and their impact on the model's output. This allows us to identify critical thresholds and guides the parameter tuning for expected behavior. In this thesis, the results were obtained mainly using this method. [75]

Another approach involves examining the system through Hopf Bifurcation analysis. It allows us to understand the stability and instability associated with the model. It is carried out to understand the transition from steady state activity to rhythmic behavior such as temporal oscillations. Hopf bifurcations are used to understand the cortex level oscillations observable on different monitoring modalities. It is typically performed using linearization and Jacobian matrix, while bifurcation diagrams are used to visualize these transitions. [75]

Turing analysis is an additional method explaining the spatial patterns resulting from state change in response to parameter shifts. It explains the emergence of patterns such as stationary fronts, pulses, waves or pulses with varying perturbations in the model. [75]

The parameters commonly known to tip the model over stabilities are noise modelled as white gaussian noise, spatial kernels, synaptic strength, and time delays. The effect of these parameters can be analyzed using the above-mentioned methods to analyze model behaviors in producing oscillations and spatial patterns. [76]

2.5 Computational Modelling of Cortical Spreading Depression Based on Neural Field Framework

There have been many attempts in modelling and simulating CSD with cell-based models, as discussed in sections 2.3.1. Neural field models as a description of spatial continuum are suitable in capturing CSD like depolarization waves. However, not many have used this approach for computational studies of CSD.

Baspinar et al. utilizing neural field model, developed a computational model to explain the mechanisms modulating CSD initiation and propagation. The model was developed to explain the role of potassium on CSD, the attribute associated with its initiation and propagation, and understanding the impact of GABAergic neurons in this event. In addition to neural interactions, reaction-diffusion equations were used to model the extracellular potassium concentration. [21]

Each neural field was represented on a 1D domain as a single unit. This discretizes the space and allows solving the equations as ordinary differential equations numerically across space. Each unit represents the interaction between excitatory and inhibitory populations modulated by potassium concentration in the extracellular space. [21]

The experimental results were derived from inducing KCL puffs to the cortical slices of mice in Baspinar et al. study. This served as the primary source of validating the model's output such as propagation speed ensuring that the model's behavior remains consistent with the physiological phenomenon. [21]

The main novelty of Baspinar et al.'s work is the addition of reaction-diffusion equation in the coupled neural field framework. The activity is mainly modulated with potassium dependent transfer functions that affect the firing of neuronal populations and the release of potassium concentration is further affected by neuronal firing. This model captures the biophysical detail required for CSD propagation while preserving the spatial dynamics required for large scale evolution, forming the rationale for its adaptation. Further details of the model and its 2D expansion are elaborated in the Materials and Methods section.

3. AIMS AND OBJECTIVES

This thesis aims to utilize population level modelling approach, more specifically neural field framework, to simulate the propagation of CSD on the cortex. The main objectives of the thesis are:

1. To extend the 1D model, developed by Baspinar et al. to model CSD, to two dimensions (2D)
2. To study the spatial patterns of the depolarization wave based on different CSD initiation regions on a 2D grid
3. To study the effects of model parameters on depolarization wave speed

The extension to a 2D space follows an assumption that the cortex can be approximated as a 2D sheet which is commonly used in neural field framework. The reason for the extension of 1D model is that a 2D representation of CSD can give rise to brain signals observed in different modalities such as EEG and MEG, making it the natural next step toward linking modelled and empirical data.

4. METHODS

In this work, a neural field model from Baspinar et al. was modified to extend it to a 2D domain. Python 3.11 was used for implementation of the model and its simulation. In this chapter, the geometry or domain where neural populations were defined is considered. The model and its building blocks are discussed in the subsequent sections in detail.

4.1 Domain

The model was implemented on a 2D patch with the assumption that CSD propagates symmetrically. The length of the patch (x -axis) and height (y -axis) were $2L$ units ranging from $-L$ to L . The number of equidistant nodes defined on the patch in x and y direction is N , each node corresponding to a neural field unit, as shown in Figure 13.

The distance between nodes is given as: $h = \frac{2L}{N-1}$

The parameters used for the domain are described in Table 1.

Table 1: Parameters used for the domain

Parameter	Value	Description
L	90	Length in x and y direction of the grid (mm)
h	3.33	Distance between nodes in x and y direction (mm)
N	3025	Number of nodes in $x = 55$ and $y = 55$ directions

The cerebral cortex has a total area of 2000 - 2300cm² folded into sulci and gyri [71]. A neural field is modelled as an idealized 2D flat sheet of cortex. The length of the field usually describes lateral connectivity i.e. connections between neurons in a cluster. A CSD wave can travel over large cortical patches ranging between 0.8 to 5.8cm² area [77]. Thus, 180mm is an approximation to capture full CSD like waves while maintaining computational efficiency. Moreover, the neuronal clusters form horizontal connections in the cortex which are 5 - 7mm long [78]. Thus, it influences number of nodes and consequently, distance between nodes. Moreover, this can be modified based on patient specific head models when moving from mesoscale to macroscale. All other parameters in this work are adapted from the work of Baspinar et al. [19]

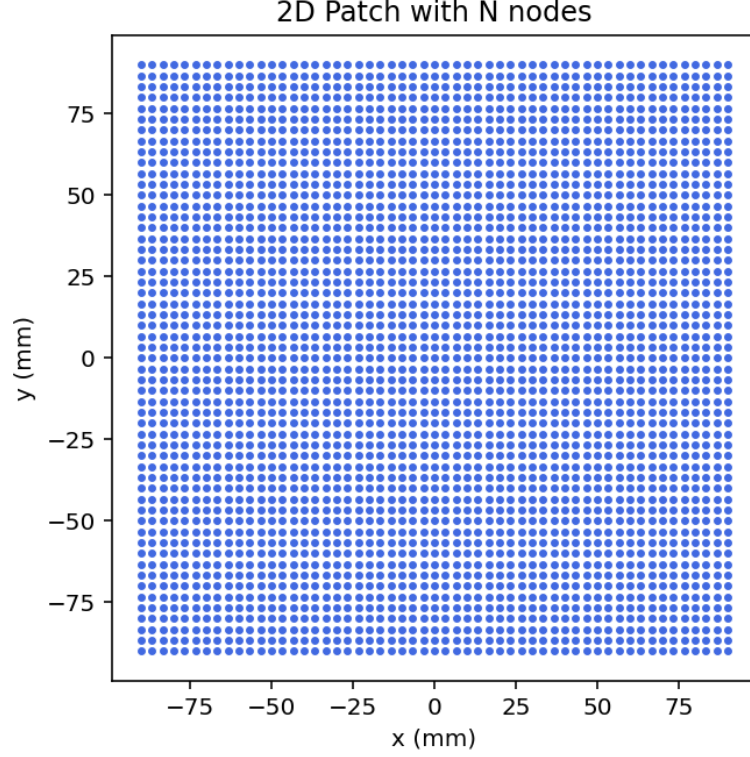


Figure 13. A 2D grid representing a 2D view of the cortex. Each blue dot is a node that represents a coupled neural field equation. Each neural field expresses excitatory and inhibitory populations in one small region of the cortex. The length of the grid is 180mm ranging from -90mm to 90mm in x and y direction.

4.2 Neural Field Model

The neural field framework describes the average activity of a neuronal population i.e. excitatory and inhibitory, based on neural field theory. The neural field equations were solved using initial value problem adaptive solver in Scipy library with Runge-Kutta Method and initial condition as 1 for all state variables. This equation of the model is described in equations 12, 13, and 14, and the model dynamics in Figure 14. The parameters are described in Table 2.

$$\tau \frac{\partial v_e}{\partial t} = -v_e + c_{ee}S_e(v_e, k) - c_{ei}S_i(v_i, k) + g_v(v_e, k) \quad (12)$$

$$\tau \frac{\partial v_i}{\partial t} = -v_i + c_{ie}S_e(v_e, k) - c_{ii}S_i(v_i, k) + g_v(v_i, k) \quad (13)$$

$$\tau \frac{\partial k}{\partial t} = \delta L_{2D} + c_1 g_k(f_e^*, f_e(v_e, k)) + c_2 g_k(f_i^*, f_i(v_i, k)) + I \quad (14)$$

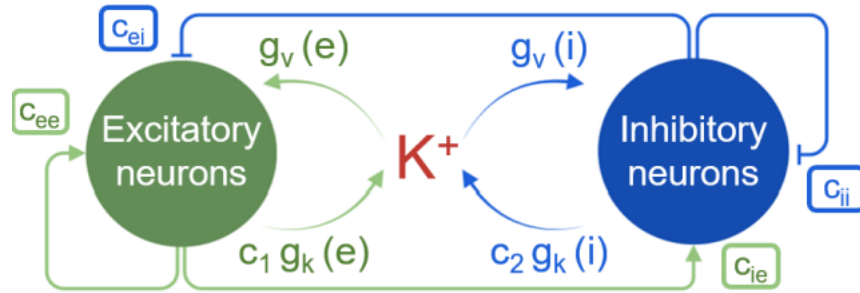


Figure 14. The connection strengths between excitatory, shown in green, and inhibitory, shown in blue, neuronal populations are given with the weights, c_{ee} , c_{ei} , c_{ie} , c_{ii} . While c_1 and c_2 are weights describing the strength of potassium release from each population. The functions g_k and g_v modulate the effects of potassium concentration on the neural populations and effect of neural population firing on extracellular potassium respectively. Image from Baspinar et al. [21]

Table 2. Parameters used for connection weights and model constants

Parameter	Value	Description
c_{ee}	1.0	Connection weight from excitatory-to-excitatory population
c_{ei}	15.0	Connection weight from excitatory to inhibitory population
c_{ie}	0.2	Connection weight from inhibitory to excitatory population
c_{ii}	15.0	Connection weight from inhibitory-to-inhibitory population
c_1	1.0	Strength weight of potassium release from excitatory population
c_2	1.3	Strength weight of potassium release from inhibitory population
δ	1	Diffusion coefficient
τ	0.3	Time constant

4.3 Model Components

In the following section, each component and its implementation of the above model is discussed.

4.3.1 State Variables

The state variables v_e and v_i describe the mean membrane potential of excitatory and inhibitory populations respectively. While k represents the potassium concentration whose diffusion or spread is given by Laplacian operator and external stimulus. In general, the model describes the effect of potassium buffering on neural populations across space. The convolution between a kernel and firing rate is multiplication in frequency domain. Therefore, to implement it, 2D Fourier Transform was taken for both the kernel and the firing rate.

4.3.2 Spatial Kernel

In neural field models, a kernel is used to define the connection between populations or units across space while firing rate is described with the transfer function mainly using a sigmoidal function. The convolution between two terms can be described by equations 15 and 16:

$$S_e(v_e, k) = \int_{2D \text{ patch}} w(x-y) f_e(v_e(y, t), k(y, t)) dy, \quad (15)$$

$$S_i(v_i, k) = \int_{2D \text{ patch}} w(x-y) f_i(v_i(y, t), k(y, t)) dy, \quad (16)$$

here $w(x-y)$ is a 2D gaussian kernel given as $w = \frac{1}{2} e(-\frac{|r|}{2\sigma^2})$ where r is a radial distance, $r = \sqrt{x^2 + y^2}$ and σ is the width equal to 2. The exponential kernel defines the connection as strongest at the origin and nearby neighbors and the weakest at large distances. The kernel is shown in Figure 15.

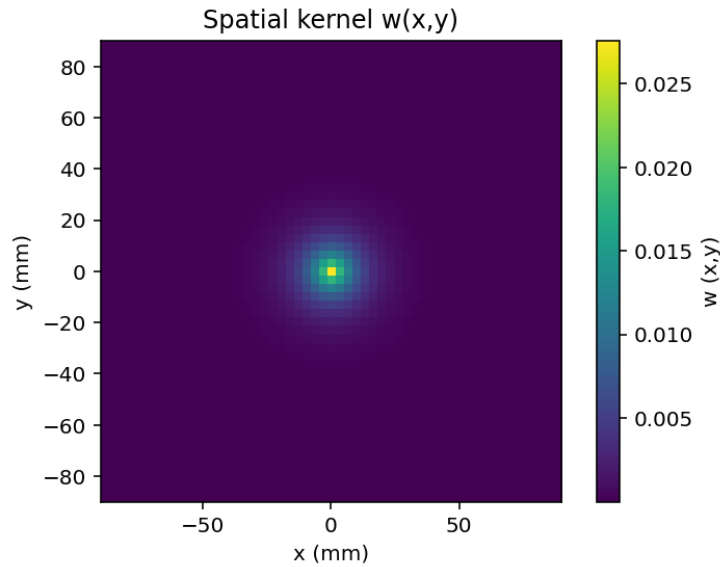


Figure 15. 2D spatial kernel of the model. The yellow region in the middle has high values representing high connectivity strength with nearby regions. The blue in the rest of the grid describes low connectivity strength as they are distant from the origin i.e. region of interest. The output of the spatial kernel is obtained after performing 2D Fourier Transform.

4.3.3 Firing Rate

In the given model, f_e and f_i are sigmoidal transfer functions for excitatory and inhibitory populations respectively. However, in Baspinar et al. model, these functions have been

altered to be dependent upon the potassium concentration to model the effect of extracellular potassium on the firing rate of a population. These conditions are given in equation 17:

$$f_{\alpha}(v, k) = \begin{cases} \frac{1}{2(1 + e^{-\beta_{\alpha}(v-h)})} = 0.5, & k < k_1^*, \\ \frac{1}{1 + e^{-\beta_{\alpha}(v-h)}} = 1, & k_1^* \leq k \leq k_2^*, \\ 0, & k_2^* < k \end{cases} \quad (17)$$

here α denotes the population, β denotes the steepness of the sigmoid, v is the membrane potential and h is the half response of the membrane potential. In the above transfer function, the model shows three conditions: normal, hyperexcitability and no activity based on potassium thresholds to simulate the CSD activity.

During normal conditions, the neurons fire at half of their maximum firing rate. However, if the potassium concentration reaches a threshold k_1^* , the neuronal population becomes hyperexcitable firing at their maximum rate, corresponding to depolarization in CSD. Moreover, if the potassium concentration keeps increasing or remains stagnant at baseline, the neurons become silent corresponding to depression of CSD. The parameters used for the firing rates are mentioned in Table 3.

Table 3. Parameters used in for firing rate transfer function for excitatory and inhibitory neurons

Parameter	Value	Description
β_e	100	Steepness of sigmoidal function for excitatory population
β_i	10	Steepness of sigmoidal function for inhibitory population
h_e	0.3	Half response of sigmoidal function for excitatory population
h_i	0.3	Half response of sigmoidal function for inhibitory population
k_{e1}^*	1.4	Potassium threshold for hyperexcitability of excitatory population
k_{e2}^*	1.8	Potassium threshold for suppression of excitatory population
k_{i1}^*	1.0	Potassium threshold for hyperexcitability of inhibitory population
k_{i2}^*	1.4	Potassium threshold for suppression of inhibitory population
v_e^*	1.5	Membrane potential for excitatory population
v_i^*	1.5	Membrane potential for inhibitory population

The output of the firing rate is demonstrated in Figure 16.

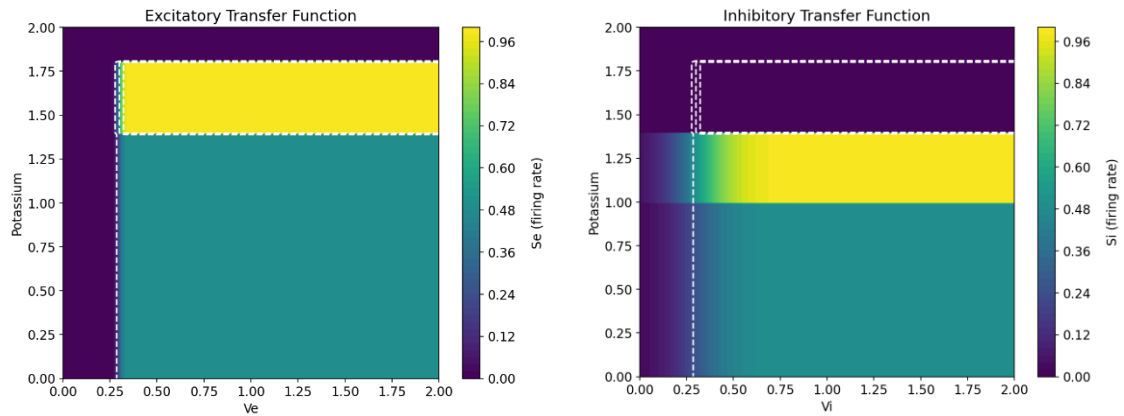


Figure 16. Potassium dependent sigmoidal transfer function for excitatory and inhibitory populations. Blue regions show no firing activity, green regions show normal firing activity, yellow regions show high firing activity. In the excitatory transfer function on the left side, neurons start firing normally at 0.25 membrane potential. Once the potassium concentration reaches 1.4, the neurons become hyperexcitable. At potassium concentration of 1.8, the neurons become silent. In the inhibitory transfer function, the thresholds for hyperexcitability and silent firing behavior is 1.0 and 1.4 respectively.

4.3.4 Effect of Potassium Concentration on Neural Population

The effect of potassium on membrane voltage of a population is defined by a generic function g_v which models how the increase in potassium concentration changes the membrane potential. This function captures all potassium related activity corresponding to ionic shifts in the neuron membrane in a phenomenological manner except the increase in potassium concentration between action potentials. This function is given as equation 18:

$$g_v(v, k) := \frac{1}{1 + e^{-\beta_v(k - k_v^*)}} = \begin{cases} 0, & k < k_v^* \\ 1, & k > k_v^* \end{cases}, \quad (18)$$

here g_v is a sigmoid function where β_v describes the steepness of the neural population's response to potassium concentration equal to, k_v^* describes the half response of the function while k is the potassium concentration. The parameter values are mentioned in Table 4:

Table 4. Parameters used in potassium function modulating neural population based on extracellular potassium concentration

Parameter	Value	Description
β_{ve}	100	Steepness of excitatory population
β_{vi}	10	Steepness for inhibitory population
k_{ve}^*	1.7	Half response for excitatory population
k_{vi}^*	1.7	Half response for inhibitory population

4.3.5 Effect of Neural Population on Potassium Concentration

When a neuron fires, it releases potassium. Now in the model, this release of potassium in between action potentials is given by the function g_k which is dependent on neuron's firing and described as equation 19:

$$g_k(s, s^*) = \frac{a}{\cosh(b(s - cs^*))}, \quad (19)$$

where $s = f_\alpha(v, k)$, $s^* = f_\alpha(v^*, k^*)$ and a, b, c are constants and their values are 3, 10, 1.5, respectively for both excitatory and inhibitory populations.

4.3.6 Laplacian Operator

The Laplacian operator in 2D space describes the spatial diffusion (divergence of the gradient) in potassium concentration with the diffusion coefficient δ . The Laplacian was solved with a finite central difference numerical method having periodic boundary conditions, as a system of linear equations. Now, in 2D space, the Laplacian can be described as the Kronecker sum of 1D discrete Laplacians [79]:

$$L_{2D} = L_x \oplus L_y = L_x \otimes I_y + I_x \otimes L_y, \quad (20)$$

where $L_x = \frac{\partial^2 k}{\partial x^2}$ along x -axis and $L_y = \frac{\partial^2 k}{\partial y^2}$ along y -axis and $I_x = I_y =$ Identity matrices.

4.3.7 Stimulus

The stimulus I is given s on the domain as a small gaussian bump to investigate the propagation of CSD. The stimulus is a mathematical approximation of KCL concentration required to initiate CSD derived experimentally in the Baspinar et al study. It is given as equation 21:

$$I(r, t) = \begin{cases} \frac{3}{\cosh^2(0.4r)}, & 2\tau \leq t \leq 4\tau, \\ 0, & \text{otherwise} \end{cases}, \quad (21)$$

where, r is the radial distance at which the stimulus is applied between 1 and 5 minutes.

The stimulus is applied at three different regions on the grid:

- Region 1: Bottom left at coordinates; $x = -70\text{mm}$, $y = -70\text{mm}$
- Region 2: Top right at coordinates; $x = 70\text{mm}$, $y = 70\text{mm}$
- Region 3: In the middle at coordinates; $x = 0$, $y = 0$

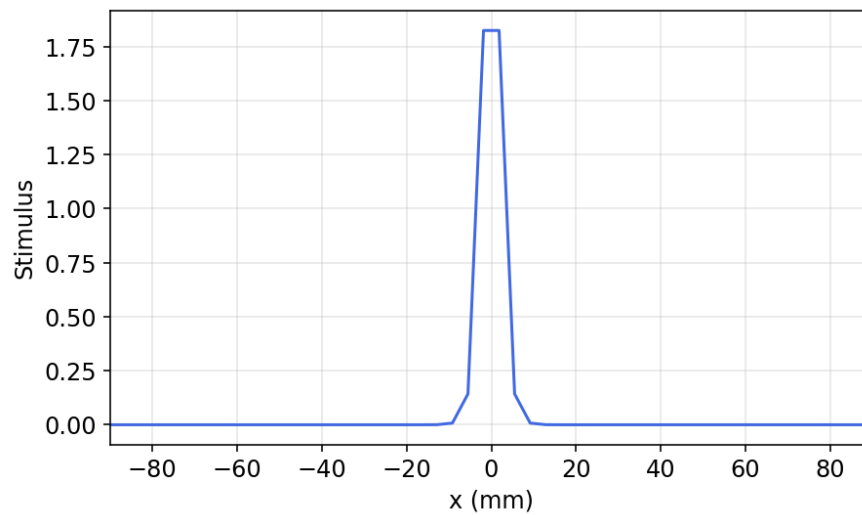


Figure 17. 1D view of applied stimulus bump in K^+ concentration at the origin. The function increases concentration for 2 to 4 mins as mentioned in equation 21.

4.4 Calculation of CSD speed

The speed of CSD is calculated by identifying the outermost neural field unit (n_{th}) that has crossed the preset wave propagation threshold (threshold = 0.91). The final velocity is calculated using the formula relating to distance and time, h defining the distance between nodes:

$$v = \frac{h * (n_{th})}{total\ time\ of\ wave\ propagation\ in\ excitatory\ population} \quad (22)$$

5. RESULTS

In this chapter, the simulated results from the developed model are provided and described. First part includes spatial and temporal dynamics while next section defines the obtained speed and impact of parameter changes on its speed. The results and their importance are examined in the Discussion section.

5.1 Spatial Distribution

The stimulus is applied to three different regions on the domain to simulate the propagation for 2 to 4 minutes. The resulting dynamics are shown in Figures 17, 18, and 19.

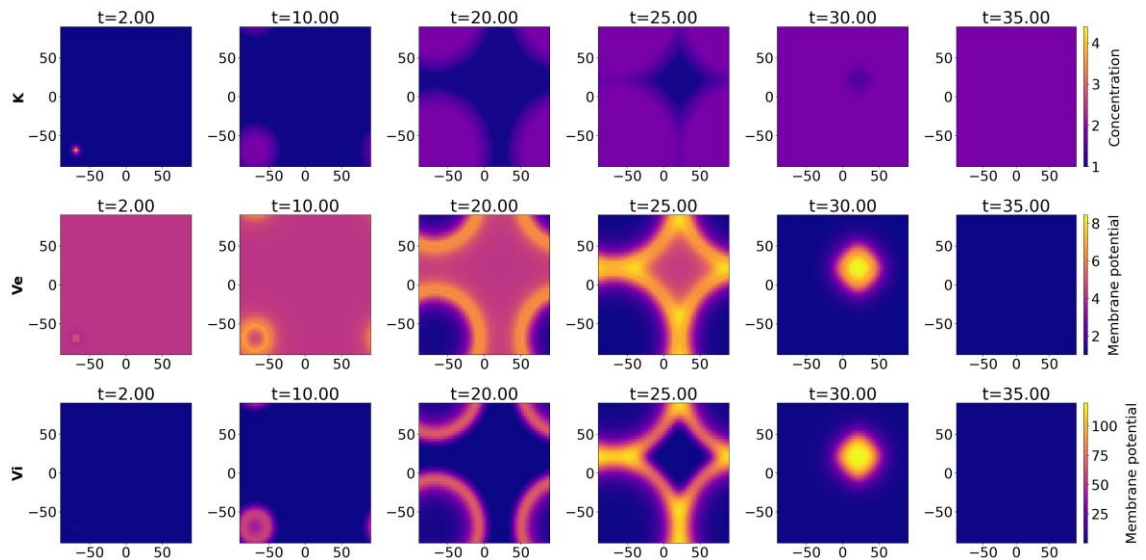


Figure 18. Region 1: Illustration of propagating CSD when stimulus is applied to bottom left corner of the domain. Each row of the plot represents the state variables K , V_e , V_i at $t = 2, 10, 20, 25, 30$ and 35 mins. The x and y axis of each subplot represents the length of the grid in x and y directions. The radial wave propagation is visible on the grid moving from left to right. In the first row, the increasing K^+ concentration is shown in purple which saturates the grid at $t = 35$. In the excitatory population, the pink color shows normal activity of the neuronal population. The orange blob shows depolarization of neuronal population in that region. The movement of depolarization along the grid is shown with increasing time. The blue region at $t = 20$ shows the silencing of excitatory neuronal populations. The wave of depolarization appears from the other side as the boundaries are wrapped with each other. The depolarization waves meet at $t = 30$. The same pattern of wave of depolarization is displayed in the inhibitory population.

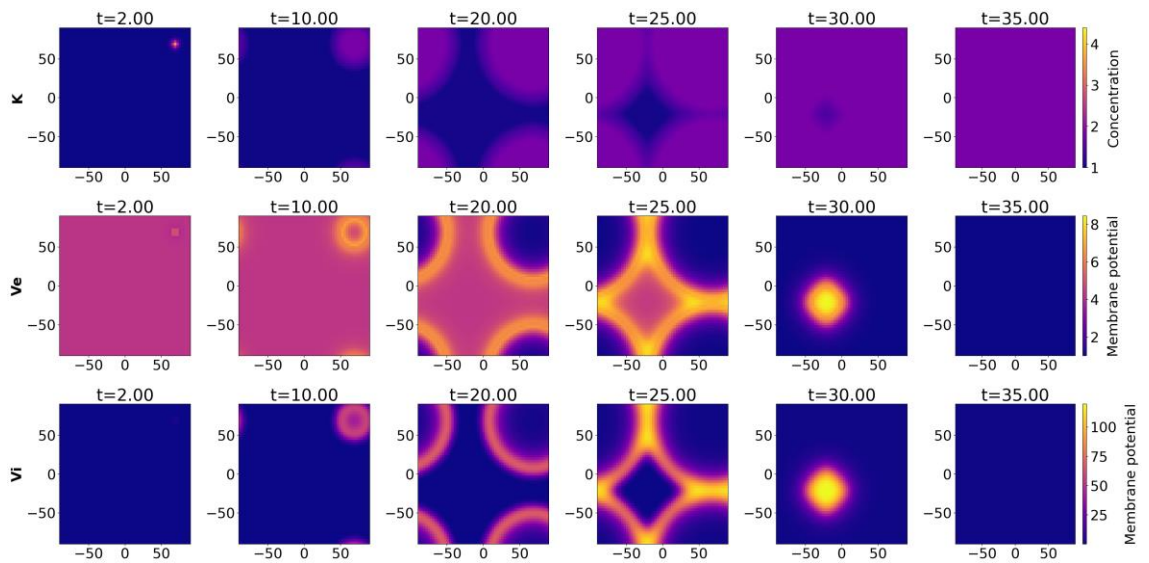


Figure 19. Region 2: Illustration of CSD propagation when stimulus is applied to top right corner of the domain. Each row of the plot represents the state variables K , V_e , V_i at $t = 2, 10, 20, 25, 30$ and 35 mins. The x and y axis of each subplot represents the length of the grid in x and y directions. The radial wave propagation from right to left is visible on the grid. The underlying dynamics are identical to Figure 18.

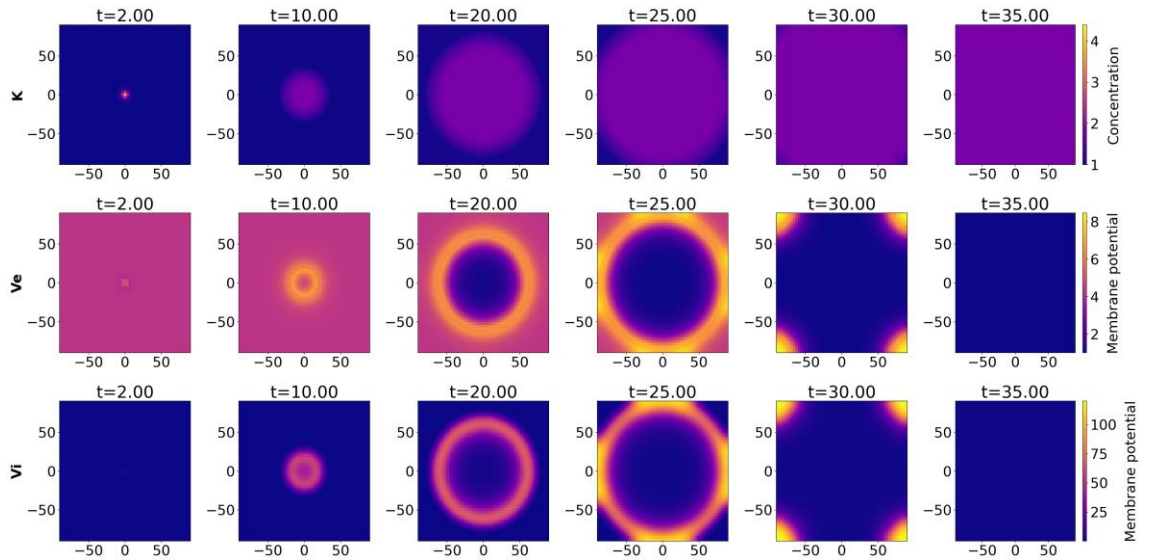


Figure 20. Region 3: Illustration of CSD propagation when stimulus is applied to the middle of the domain. Each row of the plot represents the state variables K , V_e , V_i at $t = 2, 10, 20, 25, 30$ and 35 mins. The x and y axis of each subplot represents the length of the grid in x and y directions. The radial wave propagation is visible in a ring form shown in orange on the grid propagating outward. The underlying dynamics of depolarization waves are similar as Figure 17 and 18. In the first row, the increasing $K+$ concentration is shown in purple circle. In excitatory and inhibitory populations, the blue inner circle forming at $t=20$ and propagating outwards shows the silencing of excitatory neuronal populations.

In figures 17-19, the depolarization wave, i.e., increase of membrane potential, in response to increasing potassium concentration can be observed. This wave is initiated from the region where a bump in potassium concentration is given. The potassium concentration slowly saturates the whole grid and remains stagnant after 35 mins. Meanwhile, the activity of excitatory and inhibitory populations is inhibited after the depolarization wave passes over an area.

When the stimulus is applied to top right corner of the grid, Region 1, it initiates CSD, and a curve-like pattern appears which moves along the grid from left to right. The propagation of the curve from right to left also occurs in excitatory and inhibitory populations. The formation of curvature emerges from the other end due to the periodic boundary condition which follows the assumption that the 2D grid is wrapped at boundaries to form a cortex sheet.

Similarly, when the stimulus is given to the bottom left, Region 2, the emergence of same curve like pattern can be seen. When the stimulus is applied to the middle of the grid, Region 3, the wave forms a ring like propagation moving outward.

5.2 Neuronal Firing

The mean firing across all nodes representing excitatory and inhibitory populations and node index 5 as an example is shown in Figures 21, 22, and 23.

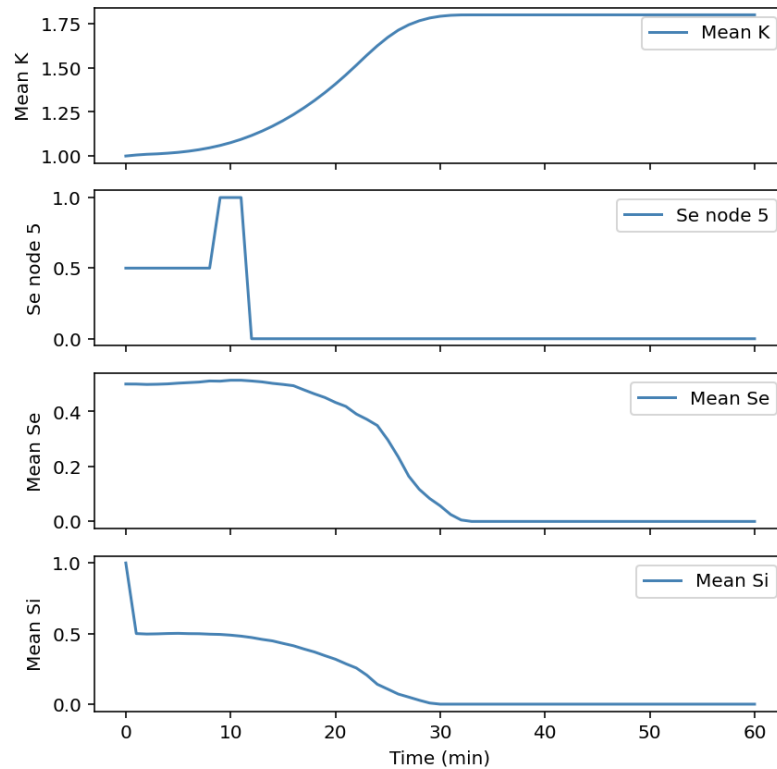


Figure 21. Region1: Mean firing rate of the domain when stimulus is applied to the bottom right corner of the domain. The x axis shows the time and y axis shows the mean firing of the whole grid. First plot shows mean potassium dynamics of the whole grid starting from 1 and reaching 1.75 with increasing time. The second plot shows the firing rate of excitatory population at node = 5. The firing starts normally with 0.5, the population becomes hyperexcitability and becomes 1 with increasing K^+ concentration at t close to 10. It stays in the same state for approximately 5 mins before becoming silent. The third plot shows mean firing of the excitatory populations of the grid. The firing starts normally from 0.5 and becomes zero at $t=32$ mins. The fourth plot shows the mean firing of the inhibitory populations of the grid in a similar manner.

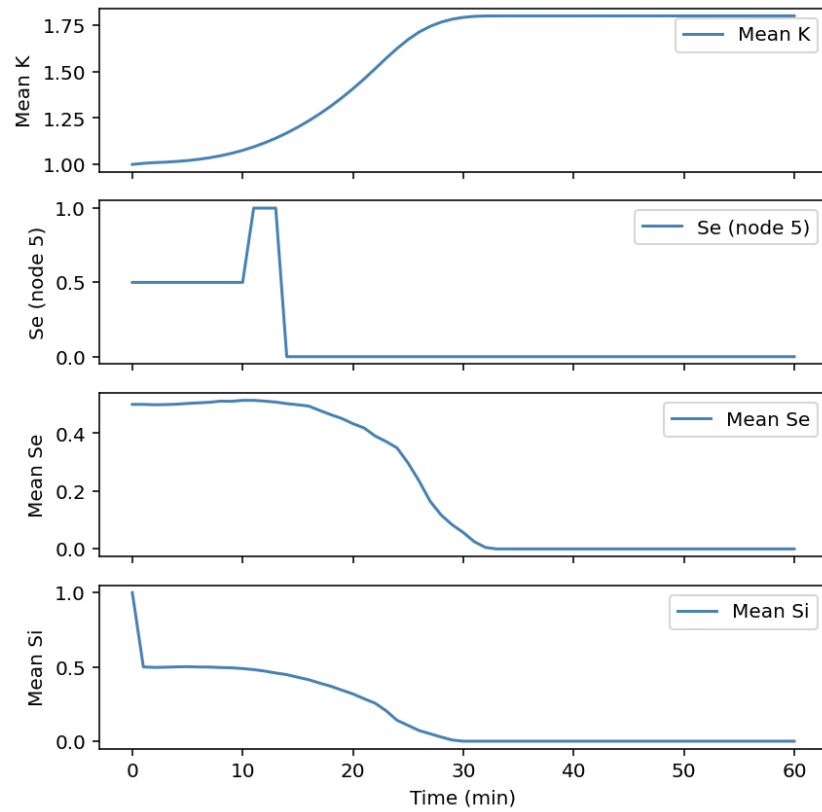


Figure 22. Region 2: Mean firing rate of the domain when stimulus is applied to the bottom right corner of the domain. The x axis shows the time and y axis shows the mean firing of the whole grid. The plot shows mean dynamics of K^+ concentration and neuronal firing of excitatory and inhibitory populations. Firing of excitatory population at node 5 is shown as a case point. The underlying dynamics are same as Figure 20.

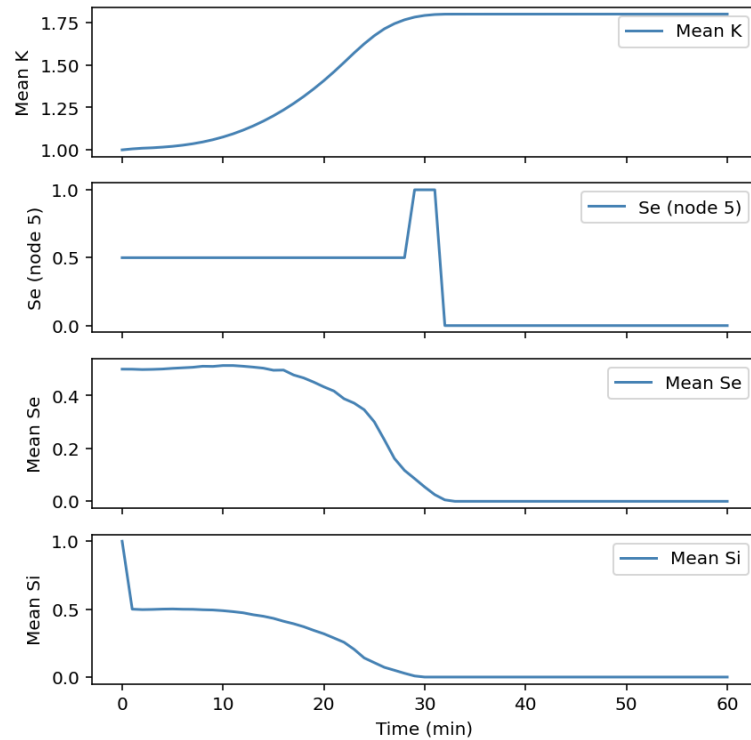


Figure 23. Region 3: Mean firing rate of the domain when stimulus is applied to the middle of the domain. The x axis shows the time and y axis shows the mean firing of the whole grid. K^+ concentration and firing dynamics of excitatory and inhibitory populations are same as Figure 20 and 21. The firing of excitatory population at node 5 starts normally at 0.5, becomes hyperexcitable and reaches 1 at $t=30$, remains hyperexcitable for few minutes and becomes silent at $t=32$.

In the figures 21 – 23, the excitatory and inhibitory populations start firing at half of their maximum firing rate on average but once the potassium reaches the silencing threshold, the firing drops to zero and remains zero for the rest of the simulation corresponding to the inhibited activity leading to suppression of neural populations in CSD. Furthermore, the depolarization time in node index 5 (situated at the top left corner on the grid) is same in the first two cases where the wave reaches in the start. However, the depolarization activity is shifted in the third case as the wave reaches it at the end.

5.3 Temporal Dynamics

The temporal progression of membrane potentials of neural populations for all three stimulus regions is plotted in Figures 23, 24, and 25. Moreover, node indices 10, 1000, 2000 and 3024 are randomly picked for illustration purposes. The net activity is derived after subtracting inhibitory mean membrane potential from excitatory mean membrane potential.

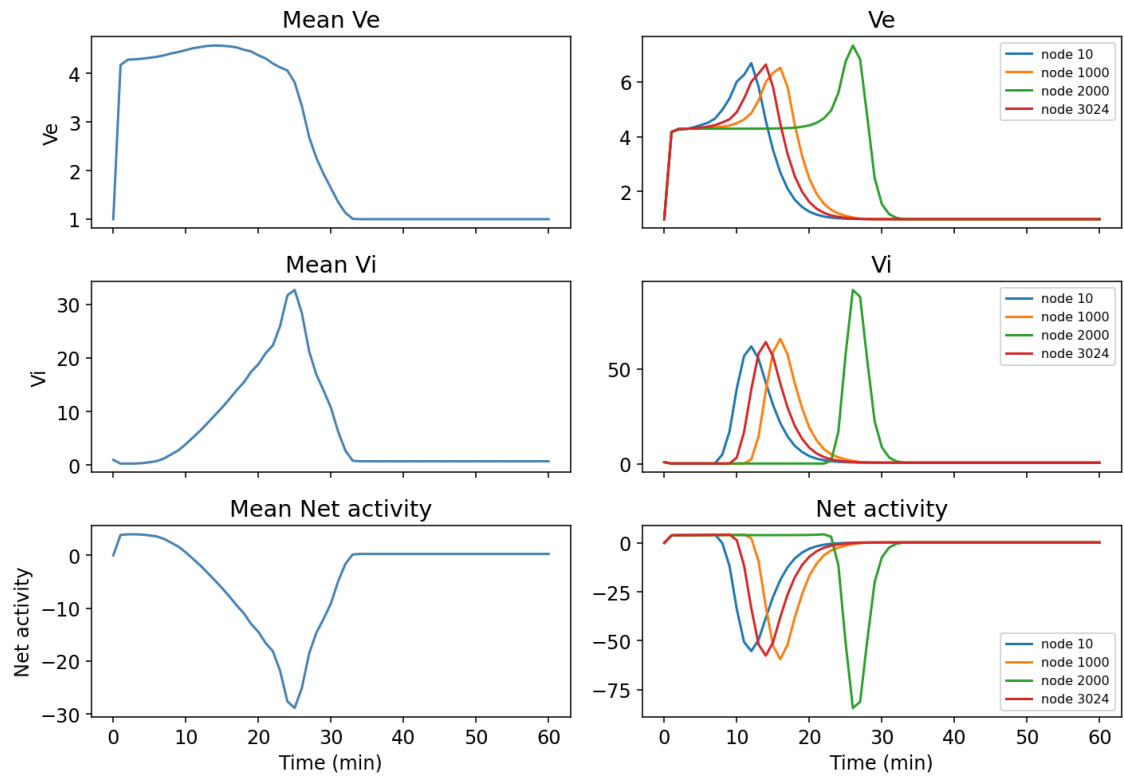


Figure 24. Region 1: Temporal activity of excitatory and inhibitory populations. Each row represents state variables as membrane potentials, V_e , V_i and Net activity obtained by subtracting V_i from V_e . Column 1 shows the mean temporal progression of neural populations on the grid. The excitatory populations stay depolarized from $t = 2$ to $t = 30$ on average. The depolarization in inhibitory populations lasts from $t=10$ to $t=32$ in minutes on average. The average net activity of the grid shows negative deflection at $t = 25$ mins. Column 2 shows the temporal progression of state variables at 4 different nodes. Depolarization times at nodes 10 (blue), 1000 (orange), 2000 (green) are approximately 10, 15, and 28 mins respectively indicating wave propagation from left to right. Depolarization time at node 3024 (red) is approximately 12 mins due to wave appearance from other side as boundaries are wrapped.

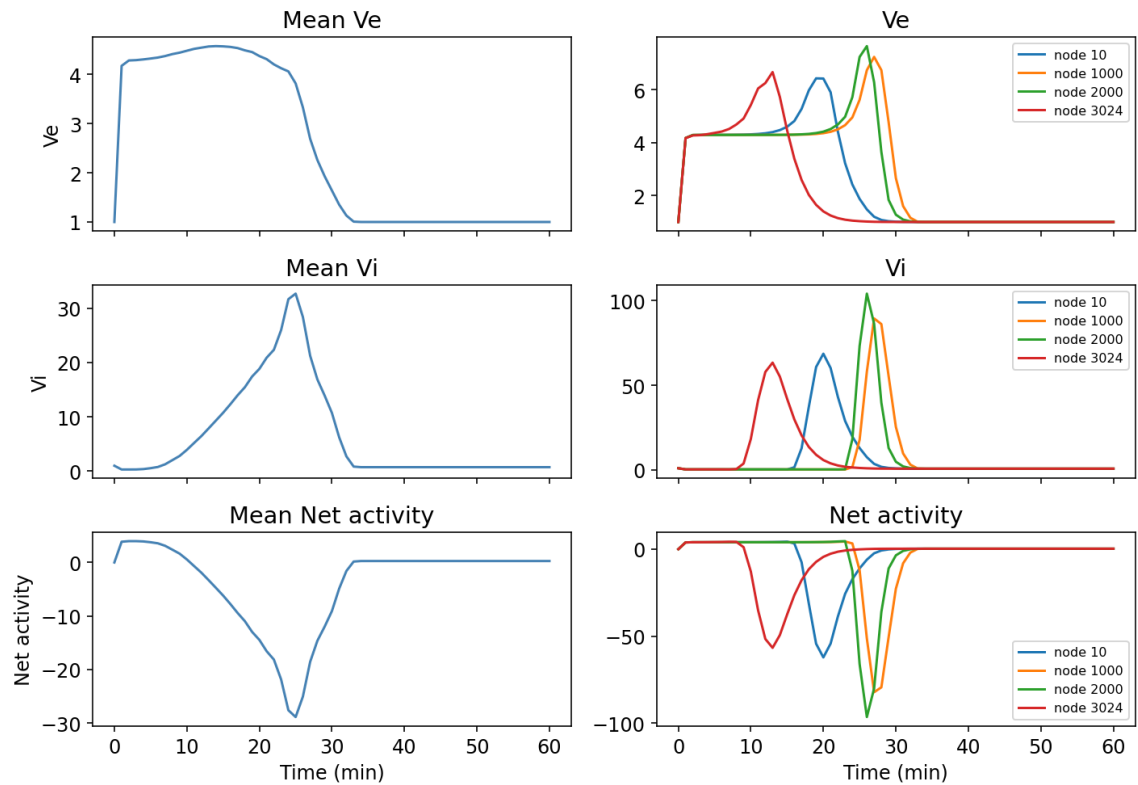


Figure 25. Region 2: Temporal activity of excitatory and inhibitory populations. Each row represents state variables as membrane potentials, V_e , V_i and Net activity obtained by subtracting V_i from V_e . Column 1 shows the mean temporal progression of neural populations on the grid, and the mean temporal progression is same as Figure 23. Column 2 in the plot represents temporal progression of state variables at 4 different nodes. Depolarization times at nodes 10 (blue), 1000 (orange), 2000 (green) are approximately 20, 28, and 25 mins respectively indicating wave propagation from right to left. Depolarization time at node 3024 (red) is approximately 12 mins due to wave appearance from other side as boundaries are wrapped.

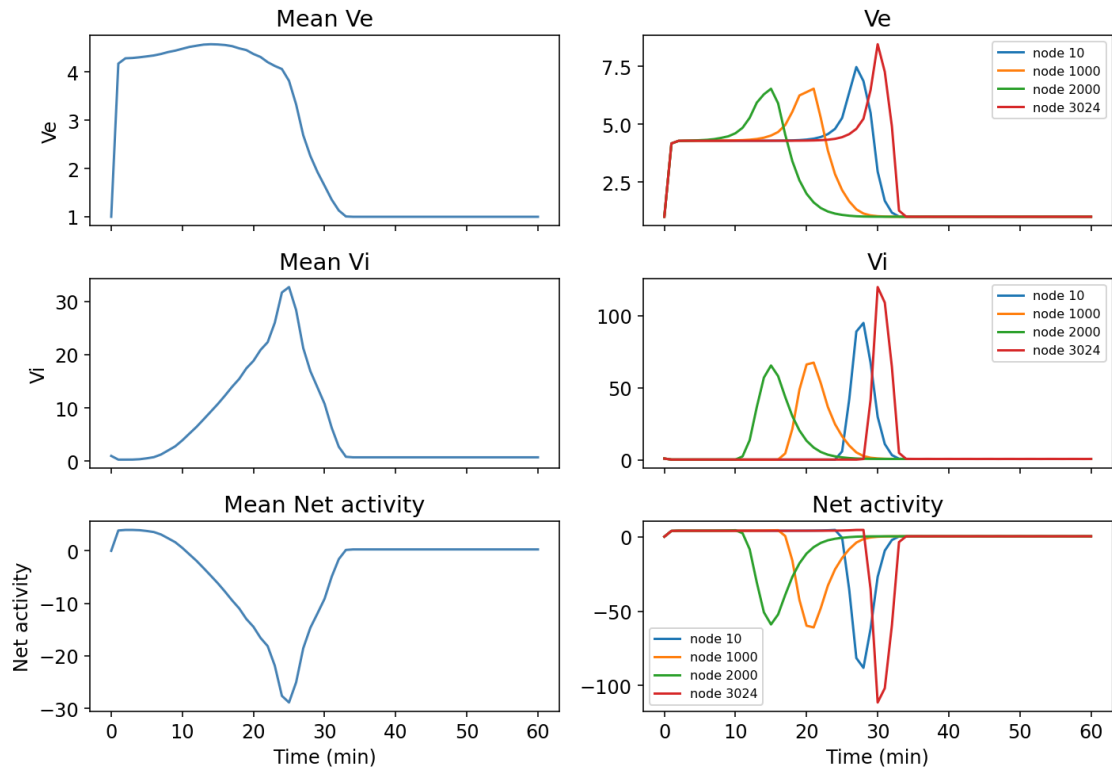


Figure 26. Region 3: Temporal activity of excitatory and inhibitory populations. Each row represents state variables as membrane potentials, V_e , V_i and Net activity obtained by subtracting V_i from V_e . Column 1 shows the mean temporal progression of neural populations on the grid, and the mean temporal progression is same as Figures 23 and 24. Column 2 in the plot represents temporal progression of state variables at 4 different nodes. Depolarization times at nodes 10 (blue), 1000 (orange), 2000 (green) are approximately 28, 20, and 15 mins respectively indicating outward wave propagation. Depolarization time at node 3024 (red) is approximately 30 mins.

In the above figures (Figures 24, 25, and 26), the mean membrane potential of excitatory population increases sharply from initial condition in response to potassium, and remains high till the wave passes, indicating overall depolarization of the domain. In contrast, the activity in each node increases and shows three phases. In the first phase, it is firing normally, once the potassium reaches a threshold of 1.4, it becomes hyper excitable and on potassium concentration reaching 1.8, it becomes silent (see Figs 21, 22, and 23 for potassium dynamics).

The mean membrane potential of inhibitory population responds to the increase in mean membrane potential of excitatory potential and gradually increases for a short period and returns to zero. As opposed to excitatory potential at different nodes, only an increase at the time points where the wave passes over them can be seen.

The mean net activity shows negative deflection at approximately $t=25$ indicating the dominance of inhibitory activity and quickly after that, all activities are returned to their baselines.

5.4 CSD Speed

Parameter analysis to find the speed corresponding to CSD was also performed. The parameters varied were time delays, number of nodes, and distance between nodes.

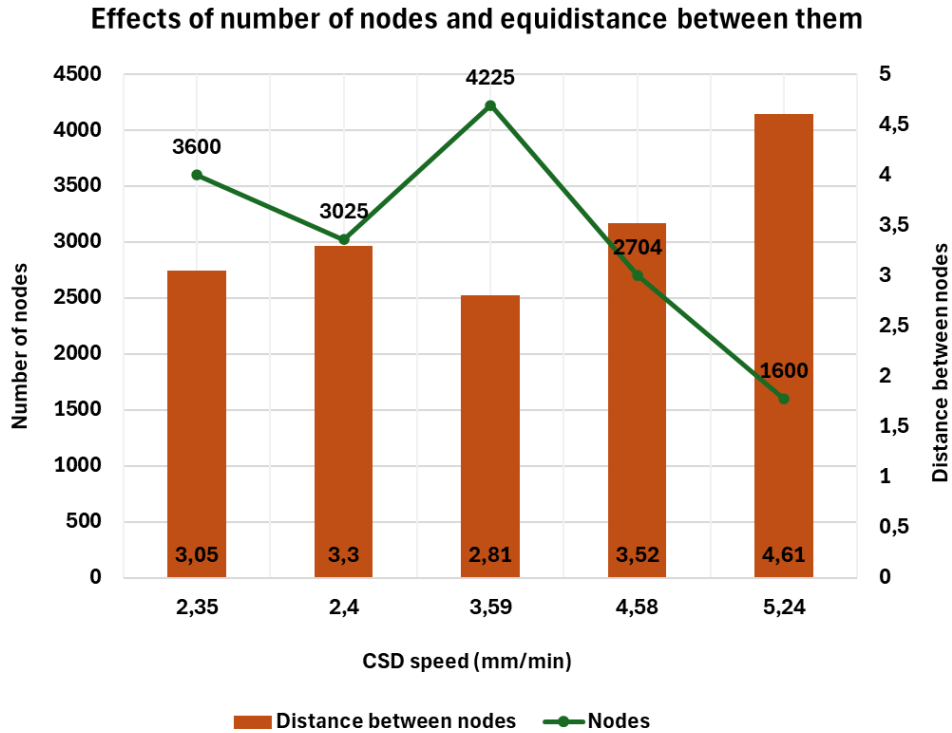


Figure 27. The graph represents CSD speed at various numbers of nodes and the distance between them. The line graph corresponds to the number of nodes while the bar graph corresponds to the distance between nodes. CSD speed of 2.35 close to control speed (2.2 mm/min) is attained with 3600 as number of nodes and 3.05mm as distant between nodes.

In Figure 27, the lowest speed was 2.35mm/min and highest speed 5.25 mm/min. The highest speed is at 1600 nodes while the lowest speed is at 3600 nodes. It is notable that with increasing number of nodes, the distance between nodes is decreasing. This is due to the fact that the length of the domain is same for all nodes. Here, the value of time delay and width of spatial kernel is same as mentioned in Materials and Methods section.

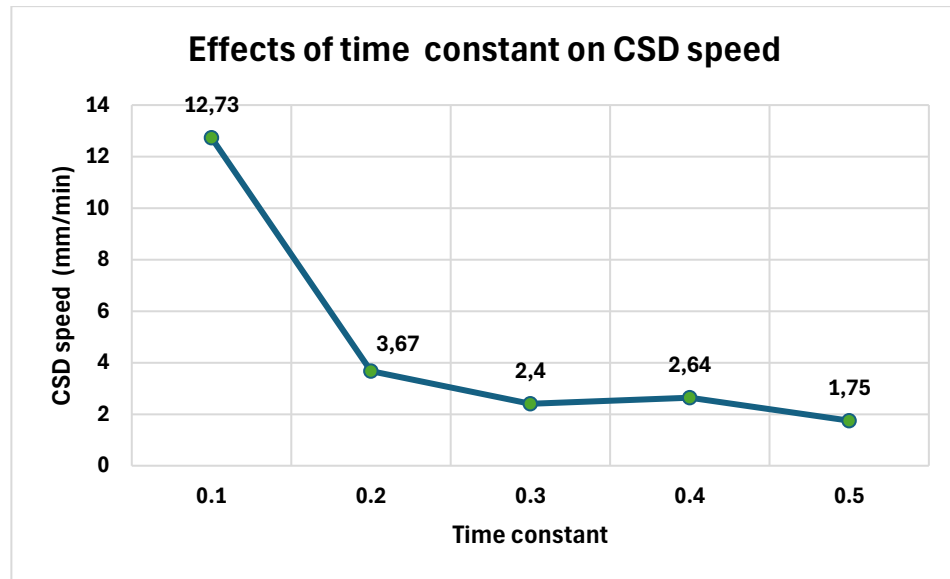


Figure 28. The graph represents the changes in speed at time delays = 0.1, 0.2, 0.3, 0.4 and 0.5. All other parameters are same as mentioned in Materials and Methods section. The CSD speed close to control speed i.e. 2.2mm/min is attained at time constant of 0.3.

In Figure 28, the lowest CSD speed was found to be 1.75 mm/min and highest to be 12.73 mm/min. Overall, a decreasing trend in speed with increasing time constants is notable.

The corresponding CSD found at different stimulus regions is shown in Figure 29.

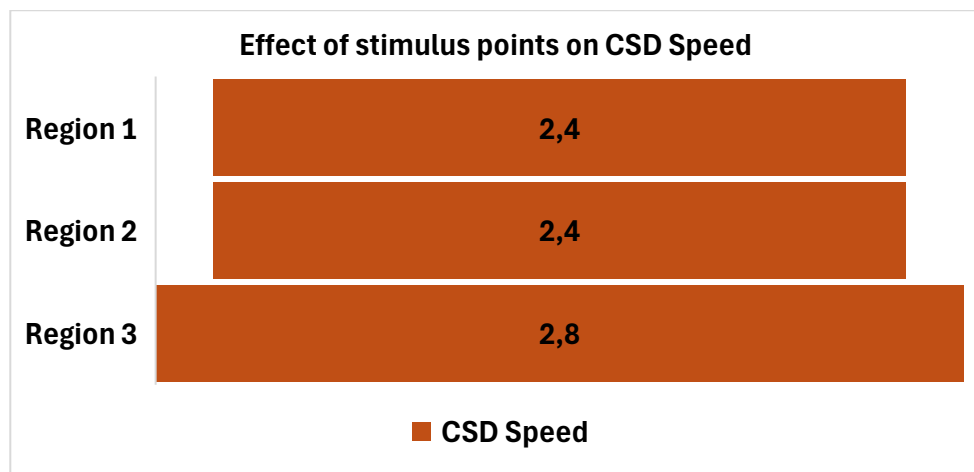


Figure 29. CSD speed observed in all three regions of applied stimulus when the parameters are same as mentioned in Materials and Methods section

6. DISCUSSION

In this work, the propagation of CSD based on neural field framework was simulated. CSD is a pathophysiological phenomenon that follows brain tissue injury as a secondary condition. It is detrimental to recovery, often exacerbates the condition and is prone to recurrence. A 2D computational model was developed from a 1D model based on neural field framework that is rooted in CSD pathophysiology.

The 1D model given by Baspinar et al. is built on Wilson-Cowen-Amari neural field framework. The novelty of their work is coupling the model with reaction-diffusion equation to model the effect the potassium concentration in the extracellular space on excitatory and inhibitory populations. Using the established model, an extension was developed to simulate CSD propagation on a 2D grid to study spatial patterns and its behavior from different initiation regions of CSD. The assumption here is that cortex can be approximated as a 2D sheet. The results of the model are validated with CSD speed derived in the experimental results obtained from rodent data [21].

The hallmark of CSD is accumulation of potassium concentrations in the extracellular space driven by firing of neurons which further depolarizes nearby neurons creating a wave of depolarization across the cortex [1]. This drive is modelled in the transfer functions of the excitatory and inhibitory populations by Baspinar et al [21]. Moreover, the increase in potassium concentration increases the neuronal firing. This feedback is modelled using another transfer function in the original 1D model [21] and employed in this work. On a 2D grid, each node represents a neural field unit corresponding to a small region of excitatory and inhibitory population on the cortex. This way, the depolarization of another neuronal population and its subsequent suppressed activity before returning to baseline is observed.

6.1 Spatial Patterns:

In the simulated results, the spatial pattern resulting from population dynamics during CSD onset can be seen. When the stimulus is applied at region 1 (bottom left corner of the grid), it initiates CSD and propagates along the grid. The stimulus point is assumed to correspond to applying stimulus to the frontal region of the cortex. The results illustrate that the potassium concentration increases from the point of stimulus and continues to increase. Moreover, the excitatory and inhibitory populations formed the depolarization

block in response to increasing potassium concentration, suppressing the activity of previous neurons.

When the stimulus is given to region 2 (top right corner of the grid), assumed to correspond to the posterior region of the cortex, the spatial distribution was same as region 1. When the stimulus is applied to region 3 (middle of the grid), assumed to correspond to the central cortex, the wave propagates outward in a circle. The spatial distribution observed in our work aligns well with CSD patterns observed in the study performed by [80,81] in 2D domain. It also indicates that our model follows the pathophysiology of CSD. The wrapping of boundaries keeps the 3D anatomical structure of the cortex intact in a 2D view.

Moreover, it is known that CSD initiates in excitatory pyramidal neurons with elevated potassium concentrations and their firing recruit inhibitory interneurons [34]. Our model captures this dynamic and shows delayed activation of inhibitory populations following excitatory neuronal firing.

6.2 Neural Firing and Temporal Patterns

Additionally, the results revealed that even though the spatial patterns differ based on CSD initiation regions, the mean firing activity and temporal evolution remained approximately the same in all three cases. The shifted increase in activity at individual nodes points to propagation of wave. Moreover, the negative deflection observed in the net activity aligns with the fact that CSD appears as a negative direct current in ECoG recordings [48].

Another important thing to note is that even though the potassium concentration does not increase after a certain threshold, the firing of excitatory and inhibited populations remains zero. This firing suggests that the inclusion of rate modulation with potassium concentration in Baspinar model [21] works correctly in our 2D model. This also corresponds to the fact that during CSD, the ability of potassium clearance is impaired by neurons [2,33]. Even though there is no further release of potassium by neurons, the impaired uptake is enough to suppress further activity.

In the computational work by [81], the inclusion of hypoxic conditions showed delayed onset of depolarization wave after giving potassium stimulus. In contrast, our model shows immediate CSD onset aligning with potassium dynamics observed in computational work of [80]. This suggests that hypoxia plays a great role in CSD depolarization wave initiation.

Overall, the resulting mean firing rate and temporal activity corresponds with the spatial dynamics and displays the model's behavior.

6.3 CSD Speed

The results were further validated by determining the CSD speed. The speed of the wave was same in the first two cases. This speed was approximately equal to the control speed obtained by the in vitro analysis in the work of Baspinar et al [21]. This speed was approximately equal to 2.2 mm/min. In the third case, the speed was slightly high showing faster spreading of CSD. This signals that spatial distribution and subsequent pattern generation have an impact on CSD speed. However, the speed still falls in the range 2-5 mm/min mentioned in the literature [1,2].

In addition, the results showed that speed can be influenced by several numerical and biophysical parameters such as time step of the simulation, synaptic time delays, number of nodes, and the distance between the node. Therefore, these parameters should be examined further.

Our results show that if the neuronal populations, on average, are slow to respond to incoming signals due to any reason i.e. larger time constant, the CSD wave propagation is slow. In contrast, if the response of the populations is fast, CSD speed is also high.

Moreover, it was found that grid resolution had a high impact on measured speed. If the grid is too sparse or too coarse, the speed of the depolarization wave was high. This indicates that the grid resolution can artificially inflate the estimation wave propagation. The normalization of the grid resolution can be explored in the future to curb this problem. This is further affected by the domain length and spatial kernel. When the grid is too coarse, even small width of the spatial kernel can be wide as it will recruit the input of more neuronal population when determining the membrane potential. Moreover, when the grid is too sparse, there are not enough grid points for calculation of membrane potentials, and each node represents a disproportionately large population resulting in high speed. This highlights the fact that fine tuning other parameters in accordance with the parameter in question is also important to avoid artefacts in wave dynamics. However, it is important to note all these values correspond to the speed observed in CSD studies.

6.4 Future work

There are many areas where this model can be utilized. For instance, the activity of neural populations can be used to estimate the voltage potentials on EEG. This can be

carried out by employing EEG forward projection method. A preliminary attempt was made to explore this aspect (see supplementary work).

In real anatomy, the brain exists in a volume in a 3D space, and the activity of neurons also exists in the 3D medium. Our model can be further extended to a 2D spherical surface, 3D volume or 3D spherical surface to model realistic anatomy of the brain and cortex. The resulting activity would give more realistic anatomical view of the neuronal activity embedded in the skull and can be projected on the scalp as EEG.

Currently, our model does not produce temporal oscillations that can be detected on the scalp suggesting a stable state of the system. This can be explained with the fact that CSD appears like a negative direct current shift on ECoG recordings which is also observable in the output of net activity in our model. However, temporal oscillations are a characteristic of dynamical systems such as neural fields and can be elicited when the parameters are tuned to find instabilities in the model. CSD appears as slow delta oscillations on a mesoscopic scale [82].

Main parameters that influence these oscillations are time constant, spatial kernel, time step of the numerical simulation, addition of noise analogous to random signals received from thalamocortical activity. For example, Mexican Hat kernel with optimum excitation inhibition balance for a general neural field model is known to shift the model from stable to unstable state. Methods such as Hopf bifurcation analysis can be utilized to find the oscillations observable on the scalp.

If CSD like slow oscillations are accomplished in the model, it would provide deeper insight into CSD dynamics and help address the current challenges faced in detection of CSD through continuous monitoring modalities (see section 2.2).

Furthermore, the model can facilitate the addition of the function of astrocytes. One of the main roles of astrocytes is to perform the clearance of potassium ions from the extracellular space. This can be achieved by including the astrocytic cell or population in the model equations modulating potassium concentration. In CSD, the role of clearing potassium concentration by astrocytes is impaired which consequently increases the potassium concentration in the extracellular space. This effect is possible to include in our 2D model.

Additionally, this model can be implemented to model other pathophysiological conditions involving potassium dynamics and wave fronts. One example of that is epilepsy, in which seizures are driven by high potassium activity producing erratic neuronal firing activity.

6.5 Limitations

One of the main limitations of neural field models is that the network is assumed to be homogenous and isotropic i.e. uniform in all directions. This assumption is not realistic biologically as the cortex is inhomogeneous and anisotropic. Moreover, the synaptic connections are modelled based on the distance between the neurons and populations. In contrast, the connections between the populations are patchy and non-uniform in real cortex. These structural variations could lead to differences in the wave speed in different directions which might not be correctly captured in the current model. [83]

The cortex has a complex anatomical structure that is folded into sulci and gyri. It also has cortical columns forming layers and microcircuit serving different sensory and motor functions. Although neural field model captures the average behavior of the cortex, it simplifies this anatomical structure as a 2D sheet which ultimately would not provide biologically realistic view of the brain function.

Even though our model is validated with wave speed obtained from experimental studies, there is still room to validate the results of the model with empirical data such as ECoG or EEG recordings.

Furthermore, our model is highly dependent on many parameters and components which increases complexity making it difficult to fully capture the whole picture of the parametric effects. Therefore, it requires systematic methods to be employed to fully study the effects of different parameters on the model. In our model, limited number of parameters are explored. Parameters such as diffusion coefficient, excitatory and inhibitory connection weights and width of the kernel are some potential candidates to understand their effect on the model's spatial and temporal output, along with their effect on CSD speed. These parameters will provide further information on potassium elevation dynamics and interactions between neural populations.

Neural field models are powerful in approximating neural activity and investigating the role of different biophysical mechanisms on the cortex level. However, there remains a tradeoff between biological details at the molecular level and computational as well as analytical tractability required to model neural dynamics at meso and macro scale.

7. CONCLUSION

The primary goal of this work was to develop a 2D extension of a computational model based on neural field framework for spreading of CSD. It is widely accepted that the main driver for CSD propagation is the sharp increase in extracellular potassium concentration. Once the initiation begins, CSD continues to spread on the cerebral cortex making it a global event.

Many techniques are used in neuroscience to develop mechanistic models for biological processes. In CSD like events, where wave dynamics are observed, spatial interactions need to be defined to accurately capture CSD propagation. Neural field framework enables to capture this with reduced dimensionality and provide interpretable description of the model.

In our results, radial wave propagation that is founded in CSD mechanism was observed. The spatiotemporal dynamics of our model show that it successfully produces neural population activity modulated with extracellular potassium concentrations. With fine tuning of a few parameters, our model produces the wave speed attributed to CSD in experimental studies, further validating our results.

Our model can be used for detecting CSD on EEG by employing forward projection method. It can also be used to perform whole brain modelling by incorporating third dimension for anatomical accuracy. Moreover, it can be used to incorporate glial cells such as astrocytes and model other neurological disorders.

Overall, this work provides a mechanistic foundation for understanding CSD and offers a computational basis for improving future detection and intervention strategies.

8. REFERENCES

- [1] Leao AAP. SPREADING DEPRESSION OF ACTIVITY IN THE CEREBRAL CORTEX. *J Neurophysiol.* 1944 Nov 1;7(6):359–90.
- [2] Lauritzen M, Dreier JP, Fabricius M, Hartings JA, Graf R, Strong AJ. Clinical Relevance of Cortical Spreading Depression in Neurological Disorders: Migraine, Malignant Stroke, Subarachnoid and Intracranial Hemorrhage, and Traumatic Brain Injury. *J Cereb Blood Flow Metab.* 2011 Jan;31(1):17–35.
- [3] Hartings JA, Bullock MR, Okonkwo DO, Murray LS, Murray GD, Fabricius M, et al. Spreading depolarisations and outcome after traumatic brain injury: a prospective observational study. *Lancet Neurol.* 2011 Dec;10(12):1058–64.
- [4] Sarrafzadeh AS, Vajkoczy P, Bijlenga P, Schaller K. Monitoring in Neurointensive Care – The Challenge to Detect Delayed Cerebral Ischemia in High-Grade Aneurysmal SAH. *Front Neurol* [Internet]. 2014 July 21 [cited 2025 Nov 25];5. Available from: <http://journal.frontiersin.org/article/10.3389/fneur.2014.00134/abstract>
- [5] Mehra A, Gomez F, Bischof H, Diedrich D, Laudanski K. Cortical Spreading Depolarization and Delayed Cerebral Ischemia; Rethinking Secondary Neurological Injury in Subarachnoid Hemorrhage. *Int J Mol Sci.* 2023 June 8;24(12):9883.
- [6] Naraoka M, Matsuda N, Shimamura N, Asano K, Ohkuma H. The Role of Arterioles and the Microcirculation in the Development of Vasospasm after Aneurysmal SAH. *BioMed Res Int.* 2014;2014:1–9.
- [7] Stragier H, Vandersmissen H, Ordies S, Thiessen S, Mesotten D, Peuskens D, et al. Pathophysiological mechanisms underlying early brain injury and delayed cerebral ischemia in the aftermath of aneurysmal subarachnoid hemorrhage: a comprehensive analysis. *Front Neurol.* 2025 May 23;16:1587091.
- [8] Charles AC, Baca SM. Cortical spreading depression and migraine. *Nat Rev Neurol.* 2013 Nov;9(11):637–44.
- [9] Dichgans M, Freilinger T, Eckstein G, Babini E, Lorenz-Depiereux B, Biskup S, et al. Mutation in the neuronal voltage-gated sodium channel SCN1A in familial hemiplegic migraine. *The Lancet.* 2005 July;366(9483):371–7.
- [10] Fabricius M, Fuhr S, Bhatia R, Boutelle M, Hashemi P, Strong AJ, et al. Cortical spreading depression and peri-infarct depolarization in acutely injured human cerebral cortex. *Brain.* 2006 Mar 1;129(3):778–90.
- [11] Strong AJ, Fabricius M, Boutelle MG, Hibbins SJ, Hopwood SE, Jones R, et al. Spreading and Synchronous Depressions of Cortical Activity in Acutely Injured Human Brain. *Stroke.* 2002 Dec;33(12):2738–43.
- [12] Dreier JP. The role of spreading depression, spreading depolarization and spreading ischemia in neurological disease. *Nat Med.* 2011 Apr;17(4):439–47.
- [13] Michael Breakspear. Dynamic models of large-scale brain activity. *Nat Neurosci.* 2017 Mar;20(3):340–52.

- [14] Depannemaecker D, Duprat C, Casagrande G, Saggio M, Athanasiadis AP, Angiolelli M, et al. A next generation neural mass model with neuromodulation [Internet]. *Neuroscience*; 2024 [cited 2025 Nov 22]. Available from: <http://bioRxiv.org/lookup/doi/10.1101/2024.06.23.600260>
- [15] Klein MO, Battagello DS, Cardoso AR, Hauser DN, Bittencourt JC, Correa RG. Dopamine: Functions, Signaling, and Association with Neurological Diseases. *Cell Mol Neurobiol*. 2019 Jan;39(1):31–59.
- [16] Kesby J, Eyles D, McGrath J, Scott J. Dopamine, psychosis and schizophrenia: the widening gap between basic and clinical neuroscience. *Transl Psychiatry*. 2018 Jan 31;8(1):30.
- [17] Breakspear M, Roberts JA, Terry JR, Rodrigues S, Mahant N, Robinson PA. A Unifying Explanation of Primary Generalized Seizures Through Nonlinear Brain Modeling and Bifurcation Analysis. *Cereb Cortex*. 2006 Sept 1;16(9):1296–313.
- [18] Phillips AJK, Robinson PA. A Quantitative Model of Sleep-Wake Dynamics Based on the Physiology of the Brainstem Ascending Arousal System. *J Biol Rhythms*. 2007 Apr;22(2):167–79.
- [19] Bojak I, Liley DTJ. Modeling the effects of anesthesia on the electroencephalogram. *Phys Rev E*. 2005 Apr 4;71(4):041902.
- [20] E. Baspinar, D. Avitabile. A neural field model for cortical spreading depression [Internet]. Available from: <https://github.com/emrebasp/A-neural-field-model-for-cortical-spreading-depression>
- [21] Baspinar E, Simonti M, Srour H, Desroches M, Avitabile D, Mantegazza M. GABAergic neurons can facilitate the propagation of cortical spreading depolarization: experiments in mouse neocortical slices and a novel neural field computational model [Internet]. *Neuroscience*; 2024 [cited 2025 Nov 22]. Available from: <http://biorxiv.org/lookup/doi/10.1101/2024.10.24.620012>
- [22] Grafstein B. MECHANISM OF SPREADING CORTICAL DEPRESSION. *J Neurophysiol*. 1956 Mar 1;19(2):154–71.
- [23] Chamanzar A, George S, Venkatesh P, Chamanzar M, Shutter L, Elmer J, et al. An Algorithm for Automated, Noninvasive Detection of Cortical Spreading Depolarizations Based on EEG Simulations. *IEEE Trans Biomed Eng*. 2019 Apr;66(4):1115–26.
- [24] Ophir O, Shefi O, Lindenbaum O. Classifying Neuronal Cell Types Based on Shared Electrophysiological Information from Humans and Mice. *Neuroinformatics*. 2024 July 8;22(4):473–86.
- [25] Zeng H, Sanes JR. Neuronal cell-type classification: challenges, opportunities and the path forward. *Nat Rev Neurosci*. 2017 Sept;18(9):530–46.
- [26] Barnett MW, Larkman PM. The action potential. *Pract Neurol*. 2007 June 1;7(3):192.
- [27] Sudhof TC. Calcium Control of Neurotransmitter Release. *Cold Spring Harb Perspect Biol*. 2012 Jan 1;4(1):a011353–a011353.

- [28] Gullledge AT, Kampa BM, Stuart GJ. Synaptic integration in dendritic trees. *J Neurobiol.* 2005 July;64(1):75–90.
- [29] Tang J, Yuan F, Shen X, Wang Z, Rao M, He Y, et al. Bridging Biological and Artificial Neural Networks with Emerging Neuromorphic Devices: Fundamentals, Progress, and Challenges. *Adv Mater.* 2019 Dec;31(49):1902761.
- [30] Hill A, Amendolara AB, Small C, Guzman SC, Pfister D, McFarland K, et al. Metabolic Pathophysiology of Cortical Spreading Depression: A Review. *Brain Sci.* 2024 Oct 16;14(10):1026.
- [31] Kager H, Wadman WJ, Somjen GG. Conditions for the Triggering of Spreading Depression Studied With Computer Simulations. *J Neurophysiol.* 2002 Nov 1;88(5):2700–12.
- [32] Tottene A, Urbani A, Pietrobon D. Role of different voltage-gated Ca²⁺ channels in cortical spreading depression: Specific requirement of P/Q-type Ca²⁺ channels. *Channels.* 2011 Mar 30;5(2):110–4.
- [33] Somjen GG. Mechanisms of Spreading Depression and Hypoxic Spreading Depression-Like Depolarization. *Physiol Rev.* 2001 July 1;81(3):1065–96.
- [34] Auffenberg E, Hedrich UBS, Barbieri R, Miely D, Groschup B, Wuttke TV, et al. Hyperexcitable interneurons trigger cortical spreading depression in an Scn1a migraine model. *J Clin Invest.* 2021 Nov 1;131(21):e142202.
- [35] Hidenori Aizawa. Spreading Depolarization Project [Internet]. 2020 Apr [cited 2025 Nov 27]. Available from: https://neurobio.hiroshima-u.ac.jp/en/project/spreading_depression-project/
- [36] Araque A, Parpura V, Sanzgiri RP, Haydon PG. Tripartite synapses: glia, the unacknowledged partner. *Trends Neurosci.* 1999 May;22(5):208–15.
- [37] Yang M fan, Ren D xue, Pan X, Li C xin, Xu S yi. The Role of Astrocytes in Migraine with Cortical Spreading Depression: Protagonists or Bystanders? A Narrative Review. *Pain Ther.* 2024 Aug;13(4):679–90.
- [38] Kros L, Lykke-Hartmann K, Khodakhah K. Increased susceptibility to cortical spreading depression and epileptiform activity in a mouse model for FHM2. *Sci Rep.* 2018 Nov 16;8(1):16959.
- [39] Ohno Y, Kunisawa N, Shimizu S. Emerging Roles of Astrocyte Kir4.1 Channels in the Pathogenesis and Treatment of Brain Diseases. *Int J Mol Sci.* 2021 Sept 23;22(19):10236.
- [40] Zhang H, Zhang X, Chai Y, Wang Y, Zhang J, Chen X. Astrocyte-mediated inflammatory responses in traumatic brain injury: mechanisms and potential interventions. *Front Immunol.* 2025 May 8;16:1584577.
- [41] Pajarillo E, Rizor A, Lee J, Aschner M, Lee E. The role of astrocytic glutamate transporters GLT-1 and GLAST in neurological disorders: Potential targets for neurotherapeutics. *Neuropharmacology.* 2019 Dec;161:107559.
- [42] Kramer DR, Fujii T, Ohiorhenuan I, Liu CY. Cortical spreading depolarization: Pathophysiology, implications, and future directions. *J Clin Neurosci.* 2016 Feb;24:22–7.

- [43] Zhou N, Gordon GRJ, Feighan D, MacVicar BA. Transient Swelling, Acidification, and Mitochondrial Depolarization Occurs in Neurons but not Astrocytes during Spreading Depression. *Cereb Cortex*. 2010 Nov;20(11):2614–24.
- [44] Ricks R, MacKenzie-Gray Scott C, Trevelyan AJ, Parrish RR. Mechanistic insight into the initiation of spreading depolarizations: Is it really all about potassium? *J Physiol*. 2025 June;603(11):3269–73.
- [45] Hsieh BY, Kao YCJ, Zhou N, Lin YP, Mei YY, Chu SY, et al. Vascular responses of penetrating vessels during cortical spreading depolarization with ultrasound dynamic ultrafast Doppler imaging. *Front Neurosci*. 2022 Nov 16;16:1015843.
- [46] Ayata C, Lauritzen M. Spreading Depression, Spreading Depolarizations, and the Cerebral Vasculature. *Physiol Rev*. 2015 July;95(3):953–93.
- [47] Maldonado-McGrath D, Sacknovitz A, Aifuwa E, Kronen S, Jain A, Calixte A, et al. Monitoring Cortical Spreading Depolarization: Advancements and Applications in Neurocritical Care: A Scoping Review. *Synapse*. 2025 July;79(4):e70021.
- [48] Hartings JA, Li C, Hinzman JM, Shuttleworth CW, Ernst GL, Dreier JP, et al. Direct current electrocorticography for clinical neuromonitoring of spreading depolarizations. *J Cereb Blood Flow Metab*. 2017 May;37(5):1857–70.
- [49] Hofmeijer J, Van Kaam CR, Van De Werff B, Vermeer SE, Tjepkema-Cloostermans MC, Van Putten MJAM. Detecting Cortical Spreading Depolarization with Full Band Scalp Electroencephalography: An Illusion? *Front Neurol*. 2018 Jan 25;9:17.
- [50] Charles A, Brennan K. Cortical Spreading Depression—New Insights and Persistent Questions. *Cephalalgia*. 2009 Oct;29(10):1115–24.
- [51] Abbott LF. Theoretical Neuroscience Rising. *Neuron*. 2008 Nov;60(3):489–95.
- [52] Gerstner W, Sprekeler H, Deco G. Theory and Simulation in Neuroscience. *Science*. 2012 Oct 5;338(6103):60–5.
- [53] Hodgkin AL, Huxley AF. A quantitative description of membrane current and its application to conduction and excitation in nerve. *J Physiol*. 1952 Aug 28;117(4):500–44.
- [54] Izhikevich EM. Simple model of spiking neurons. *IEEE Trans Neural Netw*. 2003 Nov;14(6):1569–72.
- [55] Burkitt AN. A Review of the Integrate-and-fire Neuron Model: I. Homogeneous Synaptic Input. *Biol Cybern*. 2006 July;95(1):1–19.
- [56] Aradi I, Érdi P. MULTICOMPARTMENTAL MODELING OF NEURAL CIRCUITS IN THE OLFATORY BULB. *Int J Neural Syst*. 1996 Sept;07(04):519–27.
- [57] Hines ML, Carnevale NT. The NEURON Simulation Environment. *Neural Comput*. 1997 Aug 1;9(6):1179–209.
- [58] Gewaltig MO, Diesmann M. NEST (NEural Simulation Tool). *Scholarpedia*. 2007;2(4):1430.

- [59] Stimberg M, Brette R, Goodman DF. Brian 2, an intuitive and efficient neural simulator. *eLife*. 2019 Aug 20;8:e47314.
- [60] Desroches M, Faugeras O, Krupa M, Mantegazza M. Modeling cortical spreading depression induced by the hyperactivity of interneurons. *J Comput Neurosci*. 2019 Dec;47(2–3):125–40.
- [61] Conte C, Lee R, Sarkar M, Terman D. A mathematical model of recurrent spreading depolarizations. *J Comput Neurosci*. 2018 Apr;44(2):203–17.
- [62] Shapiro BE. Osmotic Forces and Gap Junctions in Spreading Depression: A Computational Model. *J Comput Neurosci*. 2001 Jan;10(1):99–120.
- [63] Kager H, Wadman WJ, Somjen GG. Simulated Seizures and Spreading Depression in a Neuron Model Incorporating Interstitial Space and Ion Concentrations. *J Neurophysiol*. 2000 July;84(1):495–512.
- [64] Kadanoff LP. More is the Same; Phase Transitions and Mean Field Theories. *J Stat Phys*. 2009 Dec;137(5–6):777–97.
- [65] Boudec JYL, McDonald D, Munding J. A Generic Mean Field Convergence Result for Systems of Interacting Objects. In: Fourth International Conference on the Quantitative Evaluation of Systems (QEST 2007) [Internet]. Edinburgh, Scotland, UK: IEEE; 2007 [cited 2025 Nov 23]. p. 3–18. Available from: <http://ieeexplore.ieee.org/document/4338232/>
- [66] Wilson HR, Cowan JD. Excitatory and Inhibitory Interactions in Localized Populations of Model Neurons. *Biophys J*. 1972 Jan;12(1):1–24.
- [67] Li X, Li Z, Yang W, Wu Z, Wang J. Bidirectionally Regulating Gamma Oscillations in Wilson-Cowan Model by Self-Feedback Loops: A Computational Study. *Front Syst Neurosci*. 2022 Feb 21;16:723237.
- [68] Lopes Da Silva FH, Hoeks A, Smits H, Zetterberg LH. Model of brain rhythmic activity: The alpha-rhythm of the thalamus. *Kybernetik*. 1974 Mar;15(1):27–37.
- [69] Jansen BH, Rit VG. Electroencephalogram and visual evoked potential generation in a mathematical model of coupled cortical columns. *Biol Cybern*. 1995 Sept;73(4):357–66.
- [70] Wendling F, Bellanger JJ, Bartolomei F, Chauvel P. Relevance of nonlinear lumped-parameter models in the analysis of depth-EEG epileptic signals. *Biol Cybern*. 2000 Sept 6;83(4):367–78.
- [71] Cook BJ, Peterson ADH, Woldman W, Terry JR. Neural Field Models: A mathematical overview and unifying framework. *Math Neurosci Appl*. 2022 Mar 19;Volume 2:7284.
- [72] Amari S ichi. Dynamics of pattern formation in lateral-inhibition type neural fields. *Biol Cybern*. 1977;27(2):77–87.
- [73] Lomp O. Schriftliche Prüfungsarbeit für die Master-Prüfung des Studiengangs Angewandte Informatik an der Ruhr-Universität Bochum.
- [74] Coombes S. Waves, bumps, and patterns in neural field theories. *Biol Cybern*. 2005 Aug;93(2):91–108.

- [75] Bressloff PC. Spatiotemporal dynamics of continuum neural fields. *J Phys Math Theor.* 2012 Jan 27;45(3):033001.
- [76] Byrne Á, Ross J, Nicks R, Coombes S. Mean-Field Models for EEG/MEG: From Oscillations to Waves. *Brain Topogr.* 2022 Jan;35(1):36–53.
- [77] Woitzik J, Hecht N, Pinczolis A, Sandow N, Major S, Winkler MKL, et al. Propagation of cortical spreading depolarization in the human cortex after malignant stroke. *Neurology.* 2013 Mar 19;80(12):1095–102.
- [78] Pinotsis DA, Friston KJ. Neural fields, spectral responses and lateral connections. *NeuroImage.* 2011 Mar;55(1):39–48.
- [79] Al-Dweik AY, Sayyed-Ahmad A. Efficient tensor-based approach to solving linear systems involving Kronecker sum of matrices [Internet]. arXiv; 2024 [cited 2025 Nov 30]. Available from: <https://arxiv.org/abs/2410.04026>
- [80] Li B, Chen S, Li P, Luo Q, Gong H. Refractory Period Modulates the Spatiotemporal Evolution of Cortical Spreading Depression: A Computational Study. Zhang LI, editor. *PLoS ONE.* 2014 Jan 6;9(1):e84609.
- [81] Kelley C, Newton AJH, Hrabetova S, McDougal RA, Lytton WW. Multiscale Computer Modeling of Spreading Depolarization in Brain Slices. *eneuro.* 2022 July;9(4):ENEURO.0082-22.2022.
- [82] Medvedeva TM, Smirnova MP, Pavlova IV, Vinogradova LV. Different vulnerability of fast and slow cortical oscillations to suppressive effect of spreading depolarization: state-dependent features potentially relevant to pathogenesis of migraine aura. *J Headache Pain.* 2024 Jan 15;25(1):8.
- [83] Coombes S. Neural fields. *Scholarpedia.* 2006;1(6):1373.
- [84] Lecaigard F, Mattout J. Forward Models for EEG/MEG. In: *Brain Mapping* [Internet]. Elsevier; 2015 [cited 2025 Nov 30]. p. 549–55. Available from: <https://linkinghub.elsevier.com/retrieve/pii/B9780123970251003304>
- [85] MNE Python. `make_sphere_model` [Internet]. Available from: https://mne.tools/stable/generated/mne.make_sphere_model.html

9. SUPPLEMENTARY WORK

9.1 EEG Forward Projection

In the field of neuroscience, it is quite common to investigate the relationship between brain sources and neuro modalities such as EEG, MEG, fMRI etc. The techniques used to do that are of two types, forward problem when trying to predict the brain signals from neuronal activity, or inverse problem when trying to predict neuronal activity from the brain signals. In this work, forward problem or forward projection is utilized since our neuronal activity is modelled and simulated with the CSD model. The estimate of EEG signals with the neuronal activity involves three main components that describe the neuronal currents, their conducting properties from brain to the scalp and electrode information that record the signals. [84]

9.1.1 Distribution of neuronal currents

When neurons fire an action potential, the voltage of the membrane changes from resting state of -70mV. This voltage change is a result of flowing ions producing the change in currents. When the current goes into the cell, it is called a sink current and when out of the membrane, it is called source current. Now, these currents together represent transmembrane currents also known as primary currents (J_p), also producing electric fields which travel through the conductive mediums present in the brain are known as volume or secondary currents (J_e). [84]

Now the transmembrane currents are modelled using dipolar approach as the source and sink together make a dipole i.e. two opposite polarity currents separated by a small distance. In this model, each source node is represented in a 3D space elucidating dipole property whose current is given in relation to tissue conductivities (σ) and electrical field (E). [84]

$$J = J_p + J_e \quad (23)$$

or

$$J = J_p + \sigma E \quad (24)$$

9.1.2 Conduction of neuronal currents

The head is composed of many tissues, each with its own conduction properties. To model the scalp potential, these conduction properties and their relationship with the source current need to be defined. This is done using the simplification of Ohm's law, Maxwell equations and Bio-Savart law to which gives rise to the relationship between scalp potential and source activity [84]. The final equation captures how each source node contributes to the scalp potential at location (r) and time (t):

$$E(r, t) = -grad(V(r, t)) \quad (25)$$

$$\sigma(r)\nabla \cdot grad(V(r, t)) = \nabla \cdot J_p(r, t) \quad (26)$$

There are two main types of head models with conductivities, spherical models and realistic models. Spherical models have concentric shapes with homogenous and isotropic conductivities. These models are the simplest models and use analytical solutions of the above-mentioned equation. Realistic head models account for realistic head geometry with conductivities derived from MRI segmentation using Boundary Element Method (BEM). This geometry is converted into a mesh, and a numerical solution is derived using Finite Element Method (FEM) or Finite Difference Method (FDM). [84]

9.1.3 Relationship between neuronal activity and scalp potential

In real environments, EEG is captured using electrodes where each electrode sees brain activity of a specific location. To incorporate this, the names of the electrodes and their locations in head coordinates were required. Based on the head model used, the solution is calculated at each sensor location in the form of a lead field matrix. This matrix represents the pattern of how each neuronal source will be seen on the scalp and given with the following equation:

$$V = L \cdot S + \varepsilon \quad (27)$$

Where, L is the lead field matrix with $N * S$ where N is the number of electrodes, S is number of source points and ε is the measurement noise. [84]

9.2 METHOD

In this work, a 4-shell spherical model from MNE Python was used [85]. The shells correspond to brain, cerebral spinal fluid (CSF), skull and scalp. Their radius and conductivities are given on Table 5:

Table 5: Conductivities used in spherical head model by MNE Python [85]

Region	Radii (m)	Conductivities (S/m)
Brain	0.90	0.33
CSF	0.92	1.0
Skull	0.97	0.004
Scalp	1.0	0.33

The source distribution was given in a volume space where 3025 sources which were situated 8.0mm apart within 90mm radius. The sources were planted normally to cortical surface. Each source point represented the neural population node on the 2D surface. The electrode positions were defined using Biosemi-16 montage. The forward solution using MNE Python that solves the analytical solution of equation 26 at each location of electrodes in the form of a lead field matrix (L) was used.

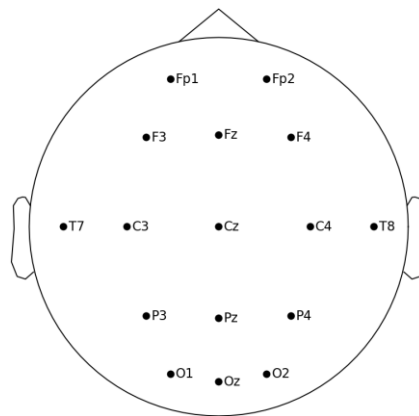


Figure 30. Montage with 16 electrodes placed on spherical head model

Since the pyramidal neurons contribute most to the EEG potentials, membrane potential from excitatory populations were used for projection.

9.3 RESULTS

The results from this projection are presented. Firstly, different levels of random noise are given to excitatory population in 2D model to visualize the effect on oscillations. The

source activity observed at each electrode is shown besides the activity obtained after adding measurement noise.

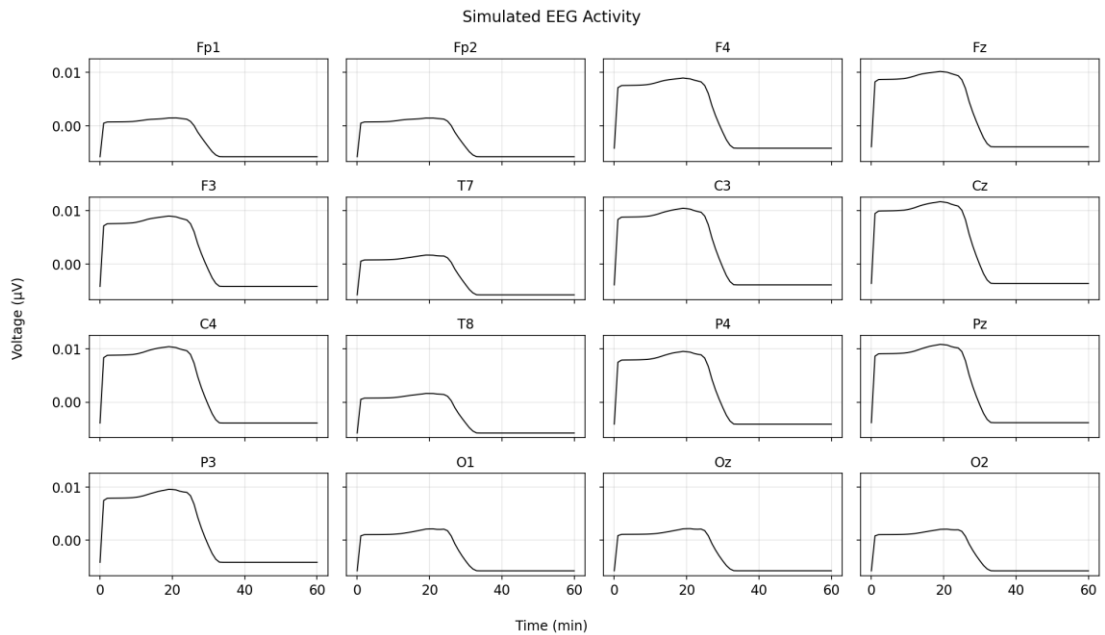


Figure 31. The plot shows simulated EEG activity at each electrode without any addition of measurement noise. Each subplot shows EEG projected on the electrode placed on the head. The x-axis at each subplot is time and y-axis is voltage in microvolts. No fluctuations are visible, and the mean pyramidal activity produced by the model (see Figures 24-26) is observable.

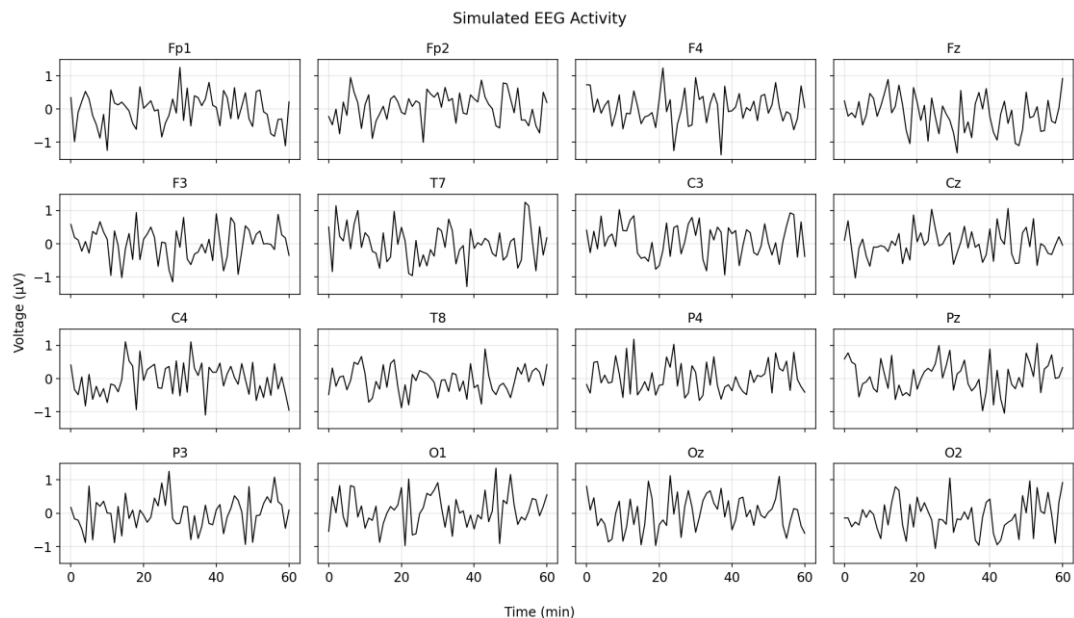


Figure 32. The plot shows simulated EEG activity at each electrode with measurement noise, added as random noise with mean = 0 and standard deviation = 5. The x-axis at each subplot is time and y-axis is voltage in microvolts. Fluctuations in the signal are visible.

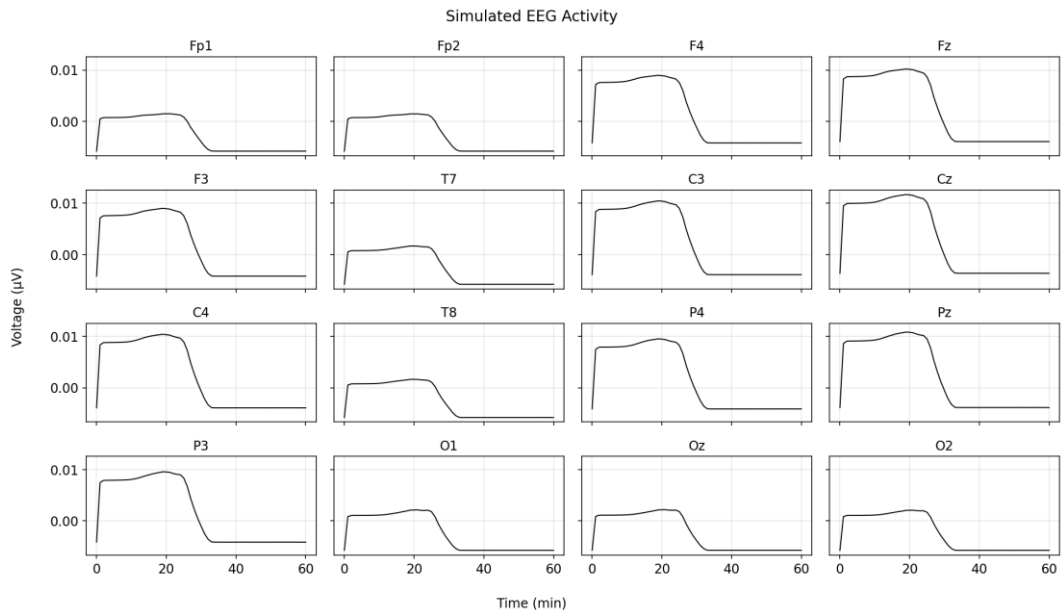


Figure 33. The plot shows simulated EEG activity at each electrode without any addition of measurement noise. Each subplot shows EEG projected on the electrode placed on the head. The x-axis at each subplot is time and y-axis is voltage in microvolts. Random noise scaled with 0.1 magnitude was added to the pyramidal populations in the model as external input. No fluctuations are visible, and the mean pyramidal activity produced by the model (see Figures 24-26) is observable at each electrode.

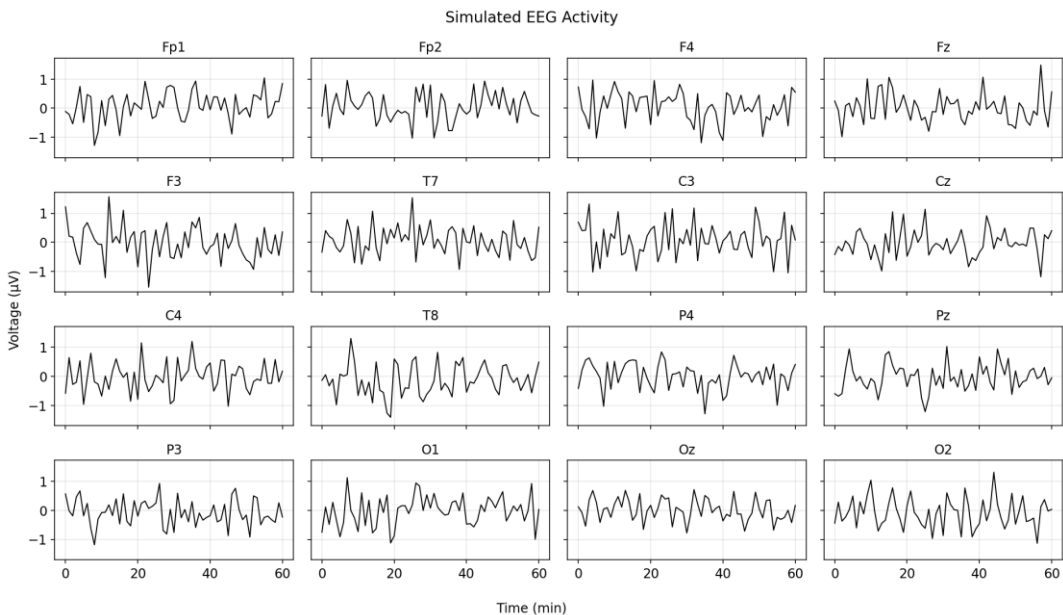


Figure 34. The plot shows simulated EEG activity at each electrode with measurement noise, added as random noise with mean = 0 and standard deviation = 5. The x-axis at each subplot is time and y-axis is voltage in microvolts. Random noise scaled with 0.1 magnitude was added to the pyramidal populations in the model as external input.

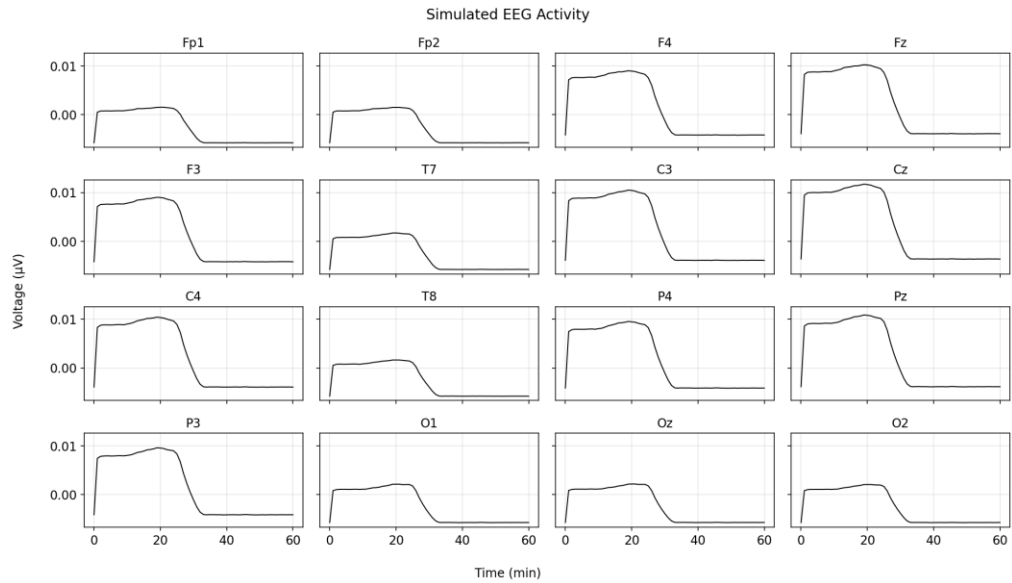


Figure 35. The plot shows simulated EEG activity at each electrode without any addition of measurement noise. Each subplot shows EEG projected on the electrode placed on the head. The x-axis at each subplot is time and y-axis is voltage in microvolts. Random noise scaled with 50 was added as external input to the pyramidal populations in the model.

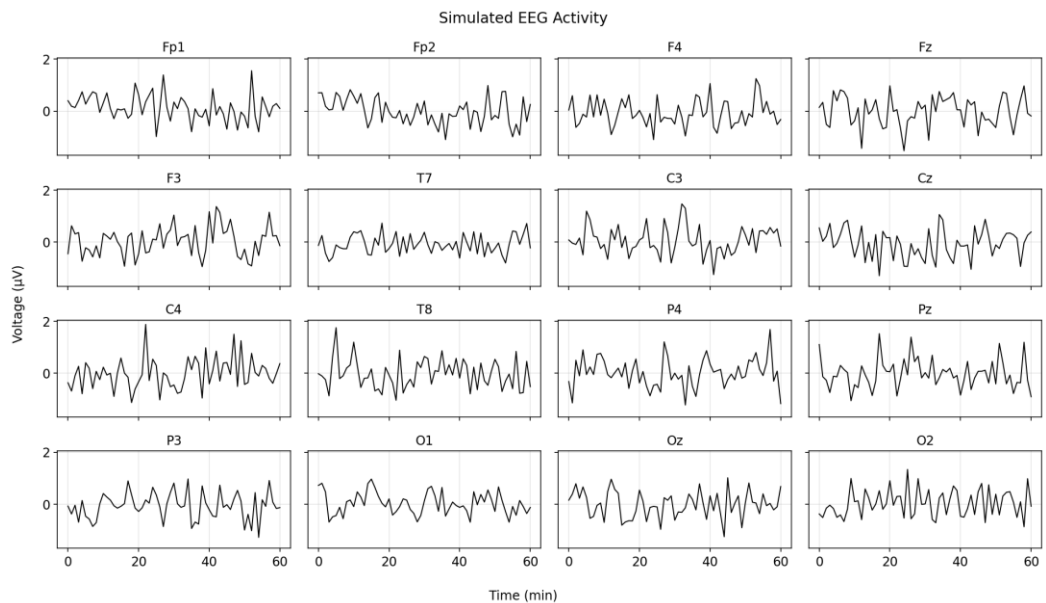


Figure 36. The plot shows simulated EEG activity at each electrode with measurement noise, added as random noise with mean = 0 and standard deviation = 5. The x-axis at each subplot is time and y-axis is voltage in microvolts. Random noise scaled with 50 magnitude was added to the pyramidal populations in the model as external input.

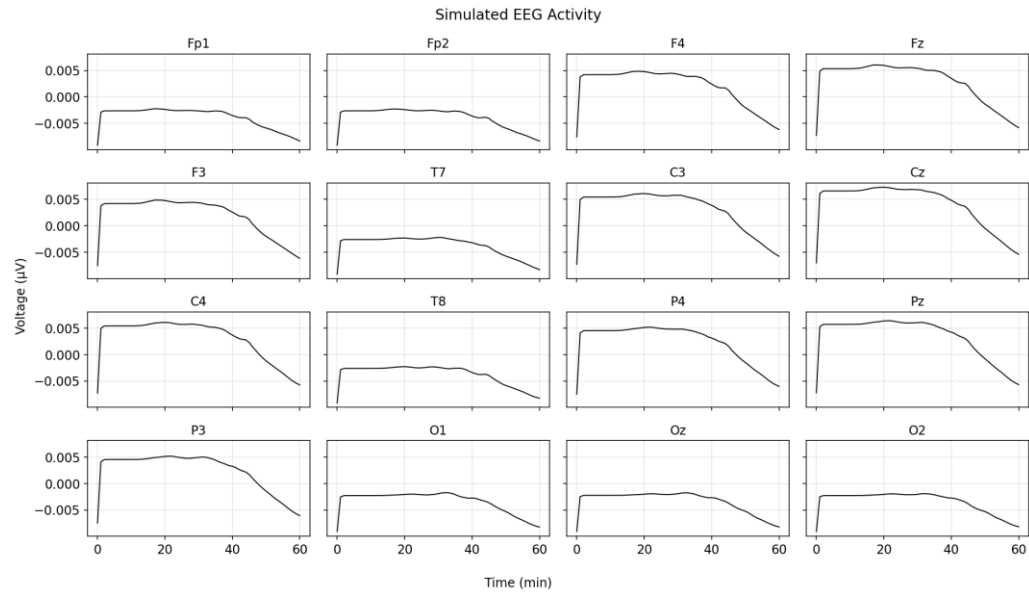


Figure 37. The plot shows simulated EEG activity at each electrode without any addition of measurement noise. Each subplot shows EEG projected on the electrode placed on the head. The x-axis at each subplot is time and y-axis is voltage in microvolts. Random noise scaled with 0.2 was added as external input to the pyramidal populations in the model. The spatial kernel was changed to Mexican hat with excitation width=2.5, inhibition width=2.0, inhibition strength=0.2, excitation strength = 1.0. There are little fluctuations but not enough to produce oscillations.

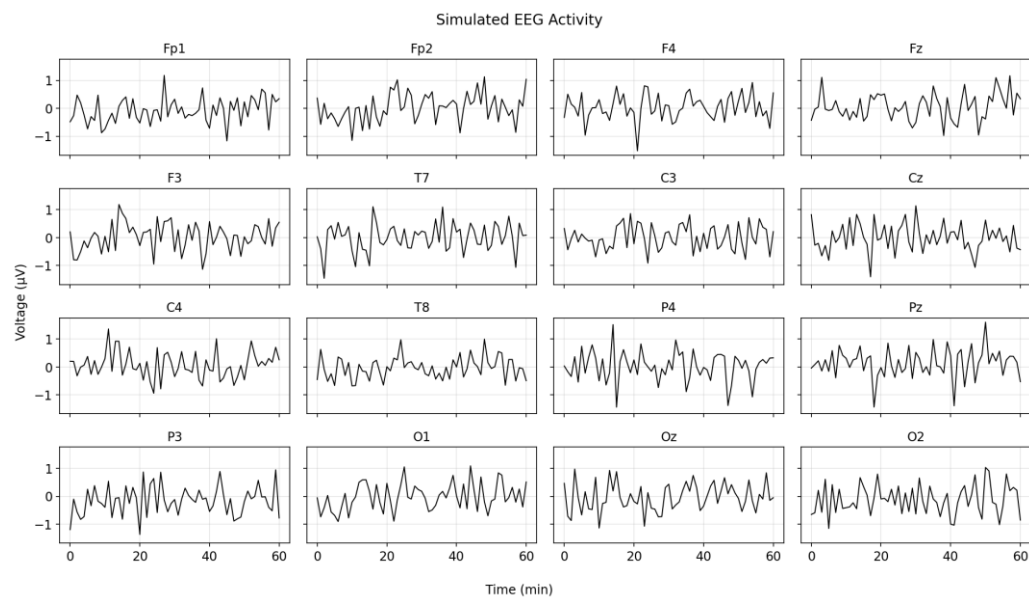


Figure 38. The plot shows simulated EEG activity at each electrode with measurement noise, added as random noise with mean = 0 and standard deviation = 5. The x-axis at each subplot is time and y-axis is voltage in microvolts. The x-axis at each subplot is time and y-axis is voltage in microvolts. Random noise scaled with 0.2 was added as external input to the pyramidal populations in the model. The spatial kernel was changed to Mexican hat with # excitation width=2.5, inhibition width=2.0, inhibition strength=0.2, excitation strength = 1.0.

The oscillatory activity is not a characteristic of current 2D model. However, the electrodes are able to capture the source activity from pyramidal population. The addition of current noise levels to pyramidal neurons and parameters of Mexican Hat kernel does not have any effect on the overall oscillatory activity of the populations. Oscillations in EEG potentials are mainly driven by measurement noise. Moreover, the propagation of CSD is not observable in the simulated EEG.